Journal of Sound and Vibration 565 (2023) 117921

Contents lists available at ScienceDirect

Journal of Sound and Vibration

journal homepage: www.elsevier.com/locate/jsvi

Beam based rotordynamics modelling for preloaded Hirth, Curvic and butt couplings

Baik Jin Kim [a], Joseph Oh [b], Alan Palazzolo [a,*]

[a] Department of Mechanical Engineering, Texas A&M University, 3123 TAMU, College Station, TX 77843, United States
[b] Hitachi America, Ltd. R&D Division, 34500 Grand River Ave, Farmington Hills, MI 48335, United States

ARTICLE INFO

Keywords:
Beam model
Young's modulus
Shear form factor
Transverse shear effect
Coupling
Greenwood Williamson (GW) contact model
Finite element method
Rotordynamics

ABSTRACT

Gas turbine and other machinery rotating assemblies are frequently manufactured as multiple components for cost and component alignment reasons. Butt joint, Hirth, and Curvic coupling are widely used for this purpose. Localized joint flexibility in these preloaded couplings introduce non-beamlike behavior which affects rotordynamic critical speeds, imbalance response and stability, rendering a conventional beam model inadequate. 3D solid finite element models of the couplings with Greenwood Williamson (GW) asperity interface features provide accurate representations of the couplings, however computational costs are impractical for use in an industrial design setting, which are limited to beam element models. A novel modeling approach for the coupling is developed that derives equivalent beam element Young's modulus and shear form factor properties, that replicate the bending behavior of the high fidelity 3D solid models, including GW based interface asperity stiffness. The equivalent beam models for butt, Hirth and Curvic couplings are validated using measured natural frequencies as a benchmark, for a range of through-bolt preloads. The equivalent beam model and the 3D solid model in this correlation incorporate GW contact models derived with experimentally measured surface roughness parameters. An $E_{coupling}$ sensitivity study for GW surface roughness parameters was conducted and showed a significant level of sensitivity. The effect of the coupling on an industrial class rotor's critical speed is included to illustrate usage of the approach.

1. Introduction

Rotating machines such as gas turbines or aero-engines are complex dynamical systems, frequently assembled with components in a stacked, preloaded assembly. The components are joined by butt joints, Hirth or Curvic couplings that facilitate assembly with precision alignment and centering capabilities. Butt joint couplings are used in the stacked rotor of the high-pressure centrifugal compressor [1]. Butt joints are smooth, toothless connections between components along the shaft, characterized by a hollow cylindrical shape. In contrast, axially preloaded high-power, gas turbine shafts may use Hirth coupling that have straight teeth, providing self-centering, high-torque transmission and clearance-free [2]. A major application of Curvic couplings is aircraft jet engine shafting [3]. The main difference between the Hirth coupling and the Curvic coupling lies in the shape of their teeth. The Curvic coupling incorporates curved-shaped teeth, with one set being convex and the other set being concave. Fig. 1 illustrates the process of manufacturing convex and concave teeth for Curvic couplings. All of these couplings possess localized contact interface flexibilities

* Corresponding author.
E-mail address: a-palazzolo@tamu.edu (A. Palazzolo).

https://doi.org/10.1016/j.jsv.2023.117921
Received 5 November 2022; Received in revised form 3 June 2023; Accepted 4 July 2023
Available online 6 July 2023

Nomenclature

FEM	finite element method
$\underline{M}$	mass matrix
$\underline{C}$	damping matrix
$\underline{C}_R$	Coriolis matrix
$\underline{C}_{b,r}$	bearing damping matrix in the rotor-fixed coordinate system
$\underline{K}$	stiffness matrix
$\underline{K}_s$	structural stiffness matrix
$\underline{K}_d$	dynamic stiffness matrix
$\underline{K}_c$	contact stiffness matrix
$\underline{K}_\sigma$	stress stiffness matrix
$\underline{K}_{b,r}$	bearing stiffness matrix in the rotor-fixed coordinate system
$\underline{F}(t)$	external force vector
$\underline{f}_c$	centrifugal force vector
$\underline{f}$	contact force vector
Ω	rotor spin speed
$\underline{q}(t)$	displacement vector
γ	shear strain
x_1	axial direction
x_2	lateral direction
u_1	displacement in x_1 direction
u_2	displacement of the neutral axis in x_2 direction
θ_3	neutral axis slope
$\hat{\tau}$	effective shear stress
G	shear modulus of elasticity
ν	Poisson's ratio.
α	ratio of inner diameter to outer diameter
A_s	effective areas
k	shear form factor
Φ	transverse shear effect
E	elastic Young's modulus
I	area moment of inertia
A	cross sectional area
L	element length of beams
$\underline{h}^e$	element contact stiffness matrix
$\underline{Ni}^e$	element inter-domain shape function matrix
$\underline{k}_c^e$	element contact stiffness coefficient matrix
k_{cn}^e	element normal contact stiffness in the $\underline{e}_n^e$ Direction
k_{ct1}^e	element tangential contact stiffness in $\underline{u}_{t1}^e$ direction
k_{ct2}^e	element tangential contact stiffness in $\underline{u}_{t2}^e$ direction
$\underline{e}_n^e$	unit normal vector of the contact plane
$\underline{e}_{t1}^e$	orthogonal vector 1 tangent to the contact plane
$\underline{e}_{t2}^e$	orthogonal vector 2 tangent to the contact plane
ns	number of nodes in contact face
n_G	number of Gauss quadrature integration points
$\xi_{1\alpha}$	Gauss quadrature point in α direction
$\xi_{2\beta}$	Gauss quadrature point in β direction
w_α	weight factor corresponding to $\xi_{1\alpha}$
w_β	weight factor corresponding to $\xi_{2\beta}$
$\underline{J}$	Jacobian matrix
R_s	average radius of asperity
η_s	area density
σ_s	standard deviation of height
$z(x)$	surface profiles
m_i	zeroth, second, and fourth spectral moments, ($i = 0, 2, 4$)
E'	Composite plane-stress modulus

P_c	contact pressure
$F_n(h)$	parabolic cylinder function
$\phi^*(s)$	Gaussian distribution function
U	Whittaker function
K	modified Bessel function of the second kind
R_a	arithmetical mean deviation
R_q	root mean square
MSE	MEAN-squared error
R^2	coefficient of determination
y_i	actual values
$\hat{y}_i$	calculated values
$\bar{y}$	mean value of y
$E_{coupling}$	Equivalent Young's modulus
OD	outer diameter
ID	inner diameter
ρ	density
$\Phi_{coupling}$	equivalent transverse shear effect
OMA	outer member sub-assembly
IMA	inner member sub-assembly
U_{md}	internal elemental strain energy due to modal deformation
$\underline{qmodal}$	modal deformation
$\underline{K_{be}}$	beam element stiffness matrix

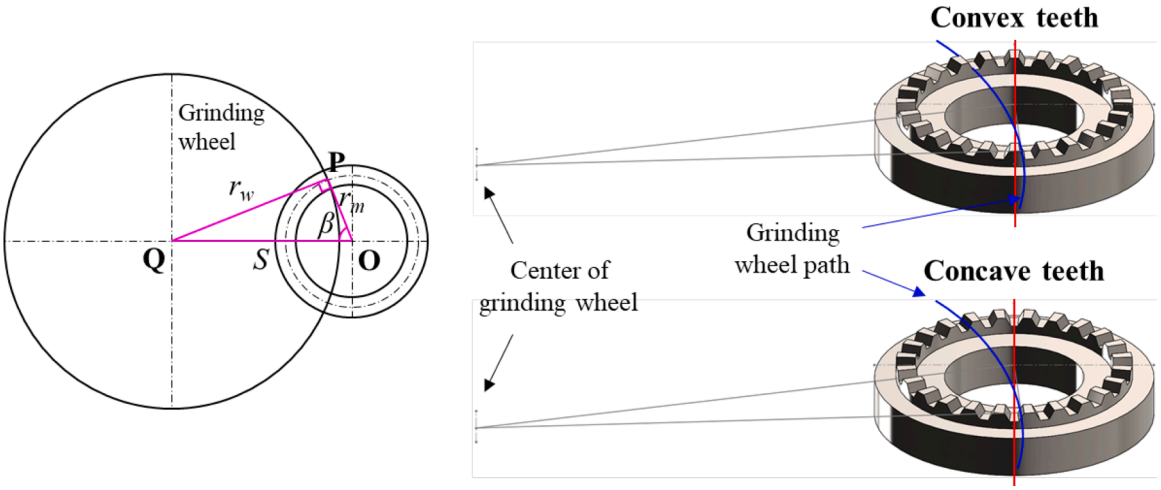

Fig. 1. Illustration of convex and concave Curvic coupling machining method [4].

resulting in a decrease in shaft lateral stiffness.

Most industrial applications use beam models for rotordynamic studies, which generally provide high accuracy for low computational cost. Stacked, preloaded rotating machinery assemblies pose a unique challenge though for beam based rotordynamic modeling, due to localized flexibilities at coupling joints. Neglect of these flexibilities using a conventional stepped beam rotordynamic model leads to overpredictions of bending natural frequencies and critical speeds [5]. This deficiency may be mitigated by using a high fidelity 3D solid, finite element model, incorporating an asperity interface model representing the preloaded joint flexibility. However, the approach is impractical when considering the extensive parametric studies required in developing a high performance machine.

A key feature of the preloaded component joint is the flexibility that arises from the asperity distribution occurring at the mating interfaces. Greenwood Williamson (GW) model [6] is one of the most reliable contact mechanics models that is frequently used to simulate the interaction between preloaded rough surfaces. There are other contact models. Chang et al. [7] developed elastic-plastic asperity volume conservation model by accounting for volume conservation of the contact region. Brake [8] developed contact models with three regimes: elastic, mixed elastic – plastic, and fully plastic. Whitehouse [9] developed their own model with autocorrelation function and found a relationship with the GW model. Although the GW model has been advanced by subsequent models it has been well tested for accuracy, and is utilized here for illustration. Gao et al. [10] employed a GW interface model for normal contact stiffness to obtain an equivalent flexural stiffness applied to contact layers. Peng et al. [11] obtained equivalent bending stiffness from GW

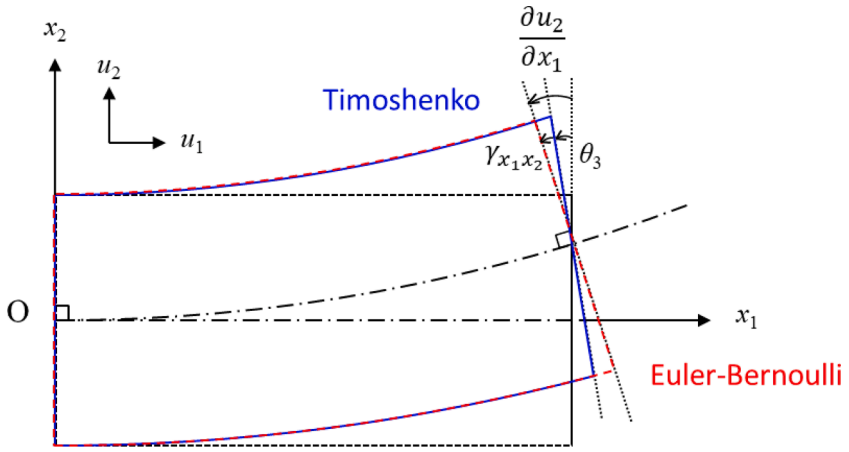

Fig. 2. Bending deformation for Euler-Bernoulli and Timoshenko beams.

contact model and used only a Timoshenko beam model to calculate critical speeds. They demonstrated that the calculated critical speed of a continuous rotor model without the contact effect is higher than with an elastic or elastic-plastic contact effect. Zhuo et al. [12] calculated the bending stiffness of contact interfaces with external bending moment and preload based on the Hertz contact theory using the GW model and the finite element method (FEM). They did not consider a curvic coupling or the use of equivalent beam elements. Kim et al. [13] used the DYNAMICS R4 beam element commercial software for modal analysis with a preload effect. A bending stiffness analysis of the joint couplings was conducted to determine an equivalent stiffness diameter for performing rotordynamic analyses Their work was limited to only beam element modeling. Liu et al. [14] obtained equivalent bending stiffness between simply supported discontinuous Timoshenko beams by using simplified torsion and shearing springs to represent the interface. External bending and shearing forces were used to calculate stiffness based on the relative displacement of the two parts. They did not use solid elements or a GW type contact model.

Researchers have considered the geometry shape effect of couplings using 3D solid finite elements. Rimpel et al. [1] used an empirically derived reduced Young's modulus of a thin element between the contact surface of a 3D butt joint model. Zhang et al. [15] used a 3D butt joint solid finite element model to explore the relationship between contact stress and contact stiffness. The latter was varied as a parameter and not based on an asperity roughness model. Croccolo et al. [16] identified the Hirth coupling features, such as tooth height h, tooth root radius r, crown clearance s, D and d for outer and inner diameters of the teeth, mean radius R_m, number of the teeth z that most heavily influence the interface bending stress. Liu et al. [17] used 3D solid elements with a nonlinear contact in three dimensions which is not based on asperity roughness, and limited elastic deformation to the coupling teeth only. The contact flexibility was represented with a uniform cylinder modeled with 3D solid elements, and with a reduced Young's modulus. Oh et al. [18] utilized 3D solid finite elements with a GW contact to model the full rotating assembly. The results clearly show the importance of contact surface roughness and applied preloads in rod-fastened rotors. Kim et al. [19] applied a 3D solid finite element with a GW contact model to a shaft with a more geometrically complicated toothed Hirth coupling. The significance of the contact surface area and the tooth number were demonstrated. Kim et al. [4] also extended this approach for curved tooth Curvic couplings, using a high-fidelity 3D solid finite element with a GW contact model.

The present study extends the previous studies on butt joints, Hirth couplings, and Curvic couplings with a GW contact model [4,18,19] to develop equivalent beam models for the couplings, that can be used in commercial beam based rotordynamic codes. The core novelty of the present work lies in obtaining the equivalent beam models for the couplings, based on outputs from high fidelity 3D finite element models including asperity interface sub-models. This provides a strong practical contribution to rotordynamics modeling practitioners that have rotor modeling software limited to beam elements, which is almost universally the case. The approach provides the Young's modulus and shear form factor constant, which are standard inputs for virtually all rotordynamics codes. The equivalent properties are derived by a matching process between the coupling's beam and high fidelity 3D solid element model predictions for the lowest two mode natural frequencies. Extensive comparisons of shaft natural frequencies are made between conventional beam models, models with equivalent beam properties, models with 3D solid element models, and measured experimental results, for Curvic, Hirth, and butt joints. The modeling methodology is illustrated with a model of an industrial class machine, demonstrating the importance of including contact stiffness in the butt, Hirth and Curvic coupling models. The influence of coupling interface surface roughness and coupling type on predicted critical speeds is investigated through parametric studies. Surface amplitude parameters are frequently used to characterize surface roughness [20]. These include arithmetical mean deviation R_a, root mean square R_q, and maximum peak to valley height of the profile R_z. Formulas are developed to provide the GW surface contact parameters needed to obtain the interface contact stiffnesses, given measured or mfg. furnished surface amplitude parameters. A procedure is presented to obtain the GW parameters from experimental measurements of surface roughness and is verified via linear regression analysis.

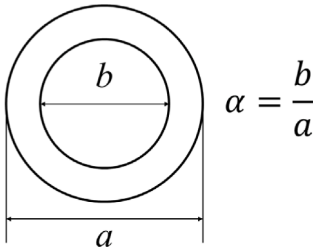

Fig. 3. Hollow cylinder cross section.

2. Finite element formulation

2.1. Beam-type finite elements

Current industrial practice for rotordynamic analyses employs beam-type FEM rotor models. The beam-type finite element rotor model is efficient and accurate for the majority of rotating machine, from fans to turbines to, compressors and even drillstring [21]. It has a capability of modeling bending, axial and torsional system has the general form.

$$\underline{M}\,\underline{\ddot{q}}(t) + \underline{C}\,\underline{\dot{q}}(t) + \underline{K}\,\underline{q}(t) = \underline{F}(t) \tag{1}$$

$\underline{M}$ is the mass matrix, $\underline{C}$ is the damping matrix, $\underline{K}$ is the stiffness matrix, $\underline{F(t)}$ is the external force vector, and $\underline{q(t)}$ is the displacement vector. Two types of beam elements are Euler-Bernoulli beam and Timoshenko. The former has a constraint that plane cross sections remain perpendicular to the neutral axis during bending, while the latter removes this assumption allowing "shear deformation". The present study uses Timoshenko beam elements, with finite element formulation of the element mass and stiffness matrices summarized in [22].

2.2. Shear form factors and transverse shear effects

Reference [23] derives the strain displacement relations and shear form factors. With reference to Fig. 2, two kinematic constraints apply to the Euler-Bernoulli beam: plane sections remain plane, and are always perpendicular to the neutral axis, which are expressed mathematically by

$$\varepsilon_{Bx_3} = -\frac{\partial}{\partial x_1}(u_1) = -\frac{\partial}{\partial x_1}\left(x_2\frac{\partial u_2}{\partial x_1}\right) = -x_2\frac{\partial}{\partial x_1}\left(\frac{\partial u_2}{\partial x_1}\right) \tag{2}$$

where u_2 is the displacement of the neutral axis in the x_2 direction.

The Timoshenko beam model allows the cross section plane to deviate from the normal direction as described by

$$\varepsilon_{Bx_3} = -x_2\frac{\partial}{\partial x_1}(\theta_3) = -x_2\frac{\partial\theta_3}{\partial x_1} \tag{3}$$

The shear strain γ in the Timoshenko beam model is

$$\gamma_{x_1x_2} = \frac{du_1}{dx_2} + \frac{du_2}{dx_1} = -\theta_3 + \frac{du_2}{dx_1} \tag{4}$$

where x_1 is the axial direction, and u_1 is the displacement in the x_1 direction. The shear strain $\gamma_{x_1x_2} = 0$ for the Euler-Bernoulli model

$$\theta_3 = \frac{du_2}{dx_1},\ \left(\gamma_{x_1x_2} = 0\right) \tag{5}$$

The shear strain varies only in the axial location, and the corresponding effective shear stress $\widehat{\tau}$ is given by

$$\widehat{\tau}_{x_1x_2}(x_1) = G\gamma_{x_1x_2}(x_1) \tag{6}$$

where G is shear modulus of elasticity. The effective shear stress can be related to the average stress by the factor k

$$\tau^{AVE}_{x_1x_2} = k\,\widehat{\tau}_{x_1x_2}(x_1) \;=\; k\,G\,\gamma_{x_1x_2}(x_1) \tag{7}$$

The shear force becomes

$$V_{x_2} = \tau^{AVE}_{x_1x_2}A = kAG\gamma_{x_1x_2}(x_1) \tag{8}$$

therefore

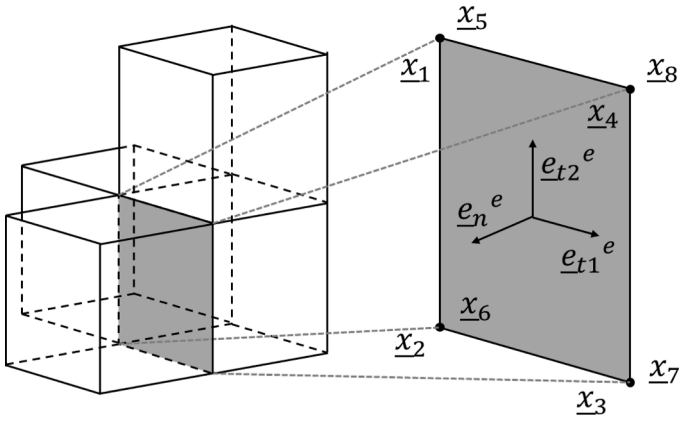

Fig. 4. Contact elements with shared interface (shaded).

$$\widehat{\tau}_{x_1x_2}(x_1) = \frac{\tau^{AVE}_{x_1x_2}}{k} = \frac{V_{x_2}}{kA} = \frac{V_{x_2}}{A_s} \tag{9}$$

where A_s is the effective areas and k is referred as shear form factor. The A_s and k changes in relation to the geometry of the cross section, e.g. for a hollow cylinder (Fig. 3), k is [24]

$$k = \frac{6(1+\nu)(1+\alpha^2)^2}{(7+6\nu)(1+\alpha^2)^2 + (20+12\nu)\alpha^2} \tag{10}$$

where ν is Poisson's ratio.

The shear form factor k can be utilized to obtain a transverse shear effect ϕ for a beam element, where E is the Young's modulus, I is the area moment of inertia, A is the cross sectional area, and L is the element length.

$$\phi = \frac{12EI}{kAGL^2} = \frac{24(1+\nu)I}{kAL^2} \tag{11}$$

The Timoshenko beam element stiffness matrix is provided from [23] in Appendix A.

2.3. Finite element formulation of contact element

An infinitesimally thin element is required to model the contact stiffness between two sub-domains sharing a common interface [25]. Fig. 4 shows two different sub-domains that are in contact. The first sub-domain consists of one hexahedron on the front whereas the second sub-domain consists of three hexahedrons on the back. The contact element sharing a common interface is shaded. The nodes $\underline{x}_1$ - $\underline{x}_4$ in the first domain correspond to the nodes $\underline{x}_5$ - $\underline{x}_8$ in the second domain, providing a conformal mesh.

The structural connection between the two domains is formed by the contact stiffness between two connecting faces. The formulation of the finite element for the contact stiffness matrix of the element is derived in [18] and the results shown below.

$$\underline{h}^e = \int_{S_e} \left(\underline{N}^e_i\right)^T k^e_c \, \underline{N}^e_i \, dS_e \tag{12}$$

$$\underline{\boldsymbol{k}}^e_{\boldsymbol{c}} = \left(\underline{\boldsymbol{e}}^e_{\boldsymbol{n}}\right)^T k^e_{cn} \, \underline{\boldsymbol{e}}^e_{\boldsymbol{n}} + \left(\underline{\boldsymbol{e}}^e_{t1}\right)^T k^e_{ct1} \, \underline{\boldsymbol{e}}^e_{t1} + \left(\underline{\boldsymbol{e}}^e_{t2}\right)^T k^e_{ct2} \, \underline{\boldsymbol{e}}^e_{t2} \tag{13}$$

$$\underline{\boldsymbol{N}}^e_{\boldsymbol{i}} = \left[\begin{array}{ccc|ccc} -N_1 & 0 & 0 & -N_{ns} & 0 & 0 \\ 0 & -N_1 & 0 \cdots & 0 & -N_{ns} & 0 \\ 0 & 0 & -N_1 & 0 & 0 & -N_{ns} \end{array}\right. \left.\begin{array}{ccc} N_1 & 0 & 0 & N_{ns} & 0 & 0 \\ 0 & N_1 & 0 \cdots & 0 & N_{ns} & 0 \\ 0 & 0 & N_1 & 0 & 0 & N_{ns} \end{array}\right] \tag{14}$$

$\underline{h}^e$ is the element contact stiffness matrix, $\underline{\boldsymbol{N}}^e_{\boldsymbol{i}}$ is the element inter-domain shape function matrix defining the displacement field across the contact plane, and $\underline{\boldsymbol{k}}^e_{\boldsymbol{c}}$ is the element contact stiffness coefficient matrix for a unit area. The term ns in $\underline{\boldsymbol{N}}^e_{\boldsymbol{i}}$ represents the number of nodes in the contact face, which is four for a hexahedron element. The matrix $\underline{\boldsymbol{k}}^e_{\boldsymbol{c}}$ can be decomposed into the element normal contact stiffness k^e_{cn} in the $\underline{\boldsymbol{e}}^e_{\boldsymbol{n}}$ direction and the element tangential contact stiffness k^e_{ct1} and k^e_{ct2} in the $\underline{\boldsymbol{e}}^e_{t1}$ and $\underline{\boldsymbol{e}}^e_{t2}$ direction, respectively. The element contact stiffness matrix in Eq. (12) is numerically integrated with Gauss quadrature [23]

$$\underline{\boldsymbol{h}}^{e} = \sum_{\alpha=1}^{n_G}\sum_{\beta=1}^{n_G} w_\alpha w_\beta \underline{\boldsymbol{N}}^{e}\left(\xi_{1\alpha},\ \xi_{2\beta}\right)^{T} \underline{\boldsymbol{k}}_{c}^{e} \underline{\boldsymbol{N}}^{e}\left(\xi_{1\alpha},\ \xi_{2\beta}\right) det\left(\underline{\boldsymbol{J}}\left(\xi_{1\alpha},\ \xi_{2\beta}\right)\right) \tag{15}$$

where n_G is the number of Gauss quadrature integration points which for 3rd order quadrature is 3 in each direction, w_α and w_β are weight factors, $\xi_{1\alpha}$ and $\xi_{2\beta}$ are Gauss quadrature integration points in the natural coordinate, and $\underline{\boldsymbol{J}}(\xi_{1\alpha},\ \xi_{2\beta})$ is the Jacobian matrix, respectively.

2.4. Equations of motion of the rotor-bearing system using 3D solid elements

The equation of motion for a rotor-bearing system modeled with 3D solid element, is written in the rotor-fixed coordinate system as [26]

$$\underline{\boldsymbol{M}}\ddot{\underline{\boldsymbol{q}}}(t) + \left\{2\Omega\underline{\boldsymbol{C}}_{\boldsymbol{R}} + \underline{\boldsymbol{C}}_{\boldsymbol{b,r}}\right\}\dot{\underline{\boldsymbol{q}}}(t) + \left\{\underline{\boldsymbol{K}}_s - \Omega^2\underline{\boldsymbol{K}}_d + \underline{\boldsymbol{K}}_c + \underline{\boldsymbol{K}}_\sigma + \underline{\boldsymbol{K}}_{\boldsymbol{b,r}}\right\}\underline{\boldsymbol{q}}(t) = \Omega^2\underline{\boldsymbol{f}}_c + \underline{\boldsymbol{f}} \tag{16}$$

where $\underline{\boldsymbol{M}}$ is the mass matrix, $\underline{\boldsymbol{C}}_{\boldsymbol{R}}$ is the Coriolis matrix, $\underline{\boldsymbol{C}}_{\boldsymbol{b,r}}$ is the bearing damping matrix in the rotor-fixed coordinate system, $\underline{\boldsymbol{K}}_s$ is the structural stiffness matrix, $\underline{\boldsymbol{K}}_d$ is the dynamic stiffness matrix, $\underline{\boldsymbol{K}}_c$ is the contact stiffness matrix, $\underline{\boldsymbol{K}}_\sigma$ is the stress stiffness matrix. The effects of stress stiffening (tensile force) or softening (compressive force) are accounted for not only at the interface but also along the entire rotor. The stress-stiffening effect on the response of a stacked rotor assembly can become significant as the preload increases. $\underline{\boldsymbol{K}}_{\boldsymbol{b,r}}$ is the bearing stiffness matrix in the rotor-fixed coordinate system, $\underline{\boldsymbol{f}}_c$ is the centrifugal force vector, $\underline{\boldsymbol{f}}$ is the contact force vector, Ω is the rotor spin speed, and $\underline{\boldsymbol{q}}(t)$ is the displacement vector. The contact stiffness matrix $\underline{\boldsymbol{K}}_c$ is obtained from Eq. (12). The detailed derivation of Eq. (16) is provided in [27].

3. Contact theory

3.1. GW contact parameters

Although a machined metal surface may appear to be smooth, surface roughness exists at the microscopic level. The GW contact model [6] was developed by Greenwood and Williamson to simulate the roughness of the surfaces that were in contact. There are three GW contact parameters that feature the surface roughness: average radius of asperity R_s, area density η_s, and standard deviation of height σ_s. These values can be obtained by measuring surface profiles z(x) and using Eqs. (17)–(23) where m_0, m_2, and m_4 are zeroth, second, and fourth spectral moments [28].

$$m_0 = mean\left(z(x)^2\right) \tag{17}$$

$$m_2 = mean\left(\left(\frac{dz(x)}{dx}\right)^2\right) \tag{18}$$

$$m_4 = mean\left(\left(\frac{d^2z(x)}{dx^2}\right)^2\right) \tag{19}$$

$$\alpha = \frac{m_0 m_4}{m_2^2} \tag{20}$$

$$R_s = \frac{3}{8}\sqrt{\frac{\pi}{m_4}} \tag{21}$$

$$\eta_s = \frac{m_4/m_2}{6\pi\sqrt{3}} \tag{22}$$

$$\sigma_s^2 = \left(1 - \frac{0.8968}{\alpha}\right)m_0 \tag{23}$$

Composite surface roughness parameters must be utilized to consider surface roughness parameters for a contact [6,29]. The spectral moments of the composite surface and the composite plane-stress modulus E' are obtained as

$$m_{n,p}^2 = m_{n,s1}^2 + m_{n,s2}^2\ \ (n = 0,\ 2,\ 4) \tag{24}$$

$$\frac{1}{E'} = \frac{1-\nu_1^2}{E_1} + \frac{1-\nu_2^2}{E_2} \tag{25}$$

where the subscripts p represents composite, the subscripts 1 and 2 represent the first and second domain at the contact face, and s1

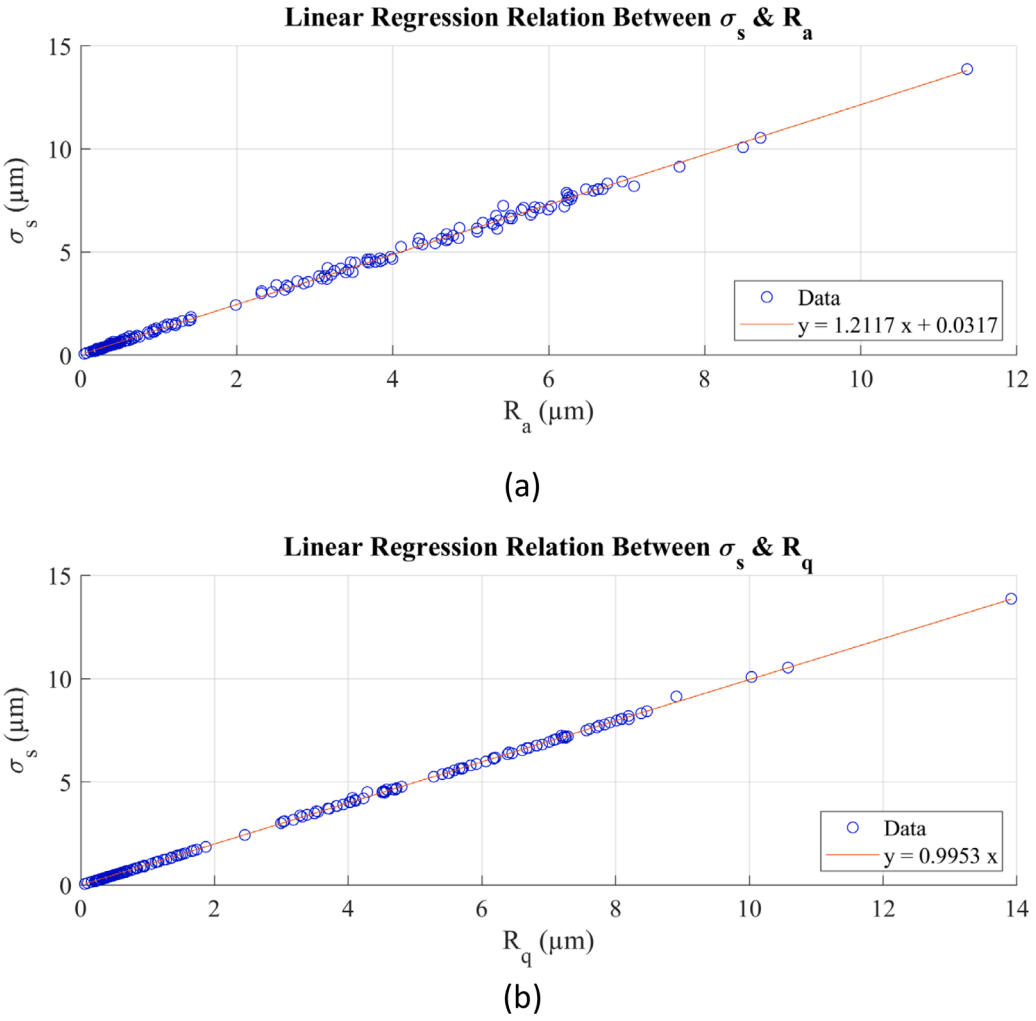

Fig. 5. Linear regression relation between (a) σ_s & R_a, and (b) σ_s & R_q.

and s2 represent surface 1 and surface 2, respectively. The contact stiffness per a unit area k_{cn} and the contact pressure P_c can be computed from the composite GW parameters using the explicit relationships shown below [6].

$$P_c = \frac{4}{3}\eta_s E' R_s^{0.5} \sigma_s^{1.5} F_{1.5}(h) \tag{26}$$

$$k_{cn} = 2\eta_s E' R_s^{0.5} \sigma_s^{0.5} F_{0.5}(h) \tag{27}$$

where h denotes the standardized separation which is defined as d/σ_s and d denotes the distance between two separated reference planes. The parabolic cylinder function is used to define $F_n(h)$.

$$F_n(h) = \int_h^\infty (s-h)^n \phi^*(s) = \frac{1}{\sqrt{2\pi}} \int_h^\infty (s-h)^n e^{-\frac{1}{2}s^2} ds = \frac{n!}{\sqrt{2\pi}} e^{-\frac{1}{2}h^2} U(n+0.5, h) \tag{28}$$

where n is either 0.5 or 1.5, $\phi^*(s)$ denotes the Gaussian distribution function, and U denotes a Whittaker function [30]. The following equations can be used to determine the terms $F_{0.5}$ and $F_{1.5}$ where K is the Modified Bessel function of the second kind [31,32].

$$U(1,x) = 2\pi^{-\frac{1}{2}} \left(\frac{1}{2}x\right)^{\frac{3}{2}} \left(-K_{\frac{1}{4}} + K_{\frac{3}{4}}\right) U(2,x) = 2 \cdot \frac{2}{3}\pi^{-\frac{1}{2}} \left(\frac{1}{2}x\right)^{\frac{5}{2}} \left(2K_{\frac{1}{4}} - 3K_{\frac{3}{4}} + K_{\frac{5}{4}}\right) \tag{29}$$

After the normal stiffness is obtained, the tangential stiffness k_{ct} can be obtained by [33]

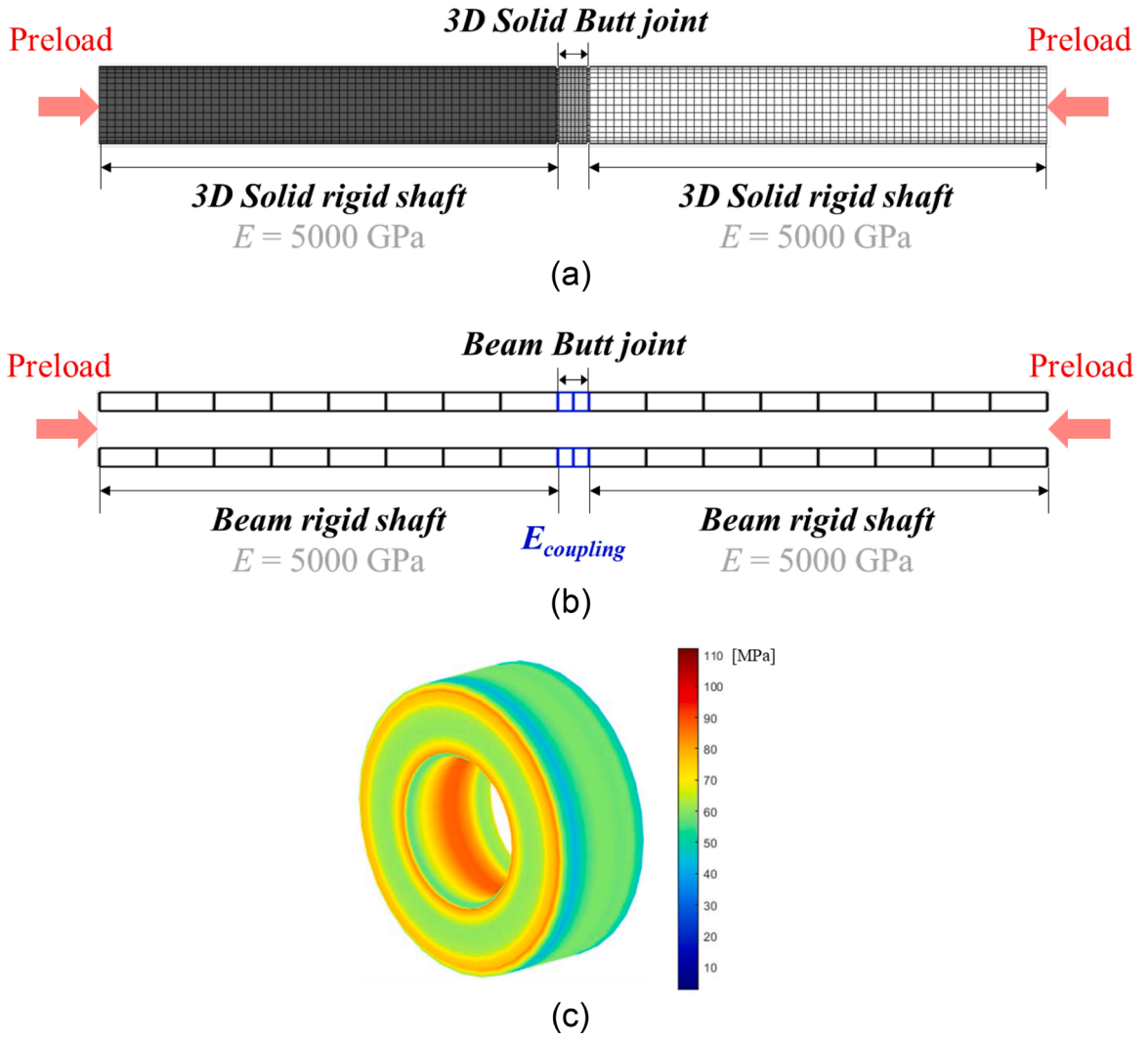

Fig. 6. Converged mesh of rigid hollow shafts and elastic butt joint assembly; (a) 3D solid element model, (b) Beam model, and (c) von Mises stress of the butt joint with axial preload of 120 kN.

$$k_{ct} = \frac{\pi(1-\upsilon)}{2(2-\upsilon)} k_{cn} \tag{30}$$

3.2. Amplitude parameters

Amplitude parameters are the most important factors in describing surface topography. The most widely utilized amplitude parameters are arithmetical mean deviation R_a and root mean square R_q. The formula for these parameters with surface profiles z(x) are [34]

$$R_a = \frac{1}{l}\int_0^l |z(x)| dx \tag{31}$$

$$R_q = \sqrt{\frac{1}{l}\int_0^l |z(x)^2| dx} \tag{32}$$

Table 1
Properties of the rigid hollow shafts and elastic butt joint assembly.

	OD [mm]	ID [mm]	L [mm]	ρ [kg/m^3]	E [GPa]	ν
Shaft	50.8	25.4	300	8202	5000	0.3
Butt joint	50.8	25.4	20.32	7800	205	0.3

Table 2
Measured composite GW parameters between the shaft and the butt joint [18].

	Composite GW contact parameters		
Surface	R_s [m]	η_s [1/m^2]	σ_s [m]
Smooth	2.8022E-06	4.9751E+10	1.5646E-06
Medium	2.0971E-06	3.5125E+10	3.3703E-06
Rough	1.5032E-06	5.0394E+10	7.0149E-06

3.3. Relationship between amplitude parameters and GW parameters

The parametric study performed in Oh et al. [18] established that among the GW contact parameters, R_s and η_s had only a minor influence on contact stiffness but σ_s had a very significant influence. Therefore, only the relationship between σ_s and R_a, and σ_s and R_q are investigated. Eqs. (17) and (32) shows that R_q equals to $m_0^{0.5}$, which provides the linear relationship

$$\sigma_s = c\ R_q \tag{33}$$

Fig. 5 shows linear regressions between σ_s and R_a, and σ_s and R_q from the experimental data in [4,18,19]. The range of measured σ_s is from 0.1 μm to 13.9 μm. A value of σ_s of 0.1 μm denotes a highly refined surface and represents an extremely smooth finish. Curvic coupling have similar surface roughness values of approximately σ_s (0.2–0.3 μm) [4]. A value of σ_s around 1 μm denotes a precision machined finish produced under controlled conditions. A value of σ_s around 10 μm represents a rough, low-grade surface roughness resulting from coarse feeds and heavy cuts. These cuts might result from milling or disk grinding. The linear regression equations shown in Fig. 5 are

$$\sigma_s = 1.2117\ R_a + 0.0317 \tag{34}$$

$$\sigma_s = 0.9953\ R_q \tag{35}$$

Mean-squared error (MSE) and coefficient of determination R^2 are computed for determining linear regressions accuracy as

$$MSE = \frac{1}{n}\sum_{i=1}^{n}(y_i - \widehat{y}_i)^2 \tag{36}$$

$$R^2 = 1 - \frac{\sum_{i=1}^{n}(y_i - \widehat{y}_i)^2}{\sum_{i=1}^{n}(y_i - \overline{y})^2} \tag{37}$$

where y_i represents the actual values, $\widehat{y}_i$ represents calculated values, and $\overline{y}$ represents the mean value of y. MSE is defined as the average squared difference between the estimated and actual values, and R^2 specifies the percentage of data points that fall within the regression equation line's outcomes. Higher R^2 indicates a strong correlation between the two variables. The MSE of the linear regression with linear R_a is 0.0157 (1.57%) while MSE of the linear regression with R_q is 0.0017 (0.17%), so both MSE are very low. R^2 of a linear regression with R_a is 0.9982 (99.82%) whereas R^2 of a linear regression with R_q is 0.9982 (99.98%), which clearly confirms the linear relationship between σ_s and R_a, and σ_s and R_q for steel-type texture amplitude distribution.

4. Equivalent beam model methodology

4.1. $E_{coupling}$: equivalent Young's modulus

This section presents an approach for incorporating the 3D solid element results into an equivalent beam element for use in conventional rotordynamic codes, employed throughout industry. Prior studies using 3D solid element models of butt joint [18], Hirth [19], and Curvic [4] couplings, with a GW contact model, showed that the natural frequencies of the shaft decrease as the applied preload decreases. This resulted from a decrease of the local lateral stiffness at coupling's contact surfaces. These results suggest tuning the Young's modulus of a beam model to match natural frequency results from a more complex 3D solid element model including the GW based contact stiffness. A method of tuning the equivalent Young's modulus is illustrated below.

Fig. 6(a) shows the 3D solid element soft butt joint model connected by two 3D solid element rigid hollow shafts, while (b) shows

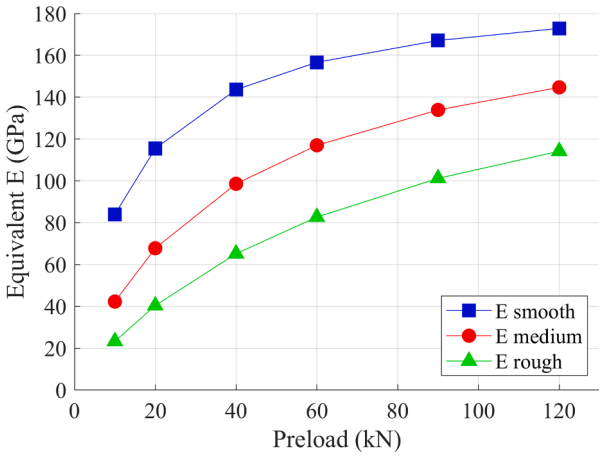

Fig. 7. $E_{coupling}$ vs. preload for different surface roughness of the butt joint.

Table 3
Composite GW parameters for sensitivity test.

	Composite GW contact parameters		
Set	R_s [m]	η_s [1/m^2]	σ_s [m]
GW1	0.1E-06	1.0E+10	1.0E-06
GW2	1.0E-06	1.0E+10	1.0E-06
GW3	10.0E-06	1.0E+10	1.0E-06
GW4	1.0E-06	0.1E+10	1.0E-06
GW5	1.0E-06	1.0E+10	1.0E-06
GW6	1.0E-06	10.0E+10	1.0E-06
GW7	1.0E-06	1.0E+10	0.1E-06
GW8	1.0E-06	1.0E+10	1.0E-06
GW9	1.0E-06	1.0E+10	10.0E-06

the beam butt joint connected by two beam rigid hollow shafts. Fig. 6(c) displays the von Mises stress plot of the butt joint when a 120 kN axial preload is applied to each end of the shaft. The geometry of the beam butt joint and the 3D solid element butt joint are identical. Table 1 lists the material properties of the rigid hollow shafts and butt joint assembly for both 3D solid and beam element models in Fig. 6. Making the adjacent hollow shafts rigid isolates the effect of the butt joint flexibility, which is of primary modeling concern for the actual rotor model that includes the butt joint. Thus, the goal is to identify an equivalent Youngs modulus solely for the beam element that models the butt joint, by matching natural frequencies. The 3D solid element rigid hollow shafts utilize the artificially high Young's modulus 5000 GPa to impose rigidity. This value of 25x actual balances the need for rigidity with avoiding ill conditioned matrices in the solution process. Table 2 lists the values of measured composite GW parameters from [18]. For three different surface roughness levels, each surface is measured ten times at various positions, yielding relative standard uncertainties ranging from 8 to 12% for the measurement surfaces.

The Young's modulus ($E_{coupling}$) of the beam butt joint shown in Fig. 6(b) is varied so that the difference between the first bending natural frequency of the beam element rigid shaft and elastic butt joint model and the 3D solid element rigid shaft- elastic butt joint model in Fig. 6 is less than 1%. The Young's modulus of the beam element rigid shaft is also set to 5000 GPa. Fig. 7 shows $E_{coupling}$ versus preload and surface roughness (from Table 2) of the butt joint, obtained in this manner. The result shows that $E_{coupling}$ increases with increasing preload for all surface roughness. This is because the local lateral stiffness at the contact faces is high when the preload is large, whereas it is relatively low when the preload is small. The result shows that $E_{coupling}$ approaches 200 GPa, which is a typical Young's modulus of steel, for the smooth roughness - high preload case. The $E_{coupling}$ has a steeper slope at low preload, allowing it to ascend quicker to 200 GPa, compared to the other roughnesses.

4.2. $E_{coupling}$ sensitivity test for GW surface roughness parameters

The sensitivity of $E_{coupling}$ to the three GW parameters from Eqs. (21)–(23) is investigated here. Nine sampled composite surface roughness are listed in Table 3. Fig. 8 shows $E_{coupling}$ versus preload for the GW parameter sets in Table 3. For GW1 to GW3, the R_s values increases by 100 times but there is only a marginal increase in $E_{coupling}$ as shown in Fig. 8(a). A similar trend occurs when η_s is increased by 100 times from GW4 to GW6. In contrast, increasing σ_s by 100 times from GW7 to GW9 shows a major decrease in $E_{coupling}$, demonstrating that $E_{coupling}$ is most sensitive to σ_s.

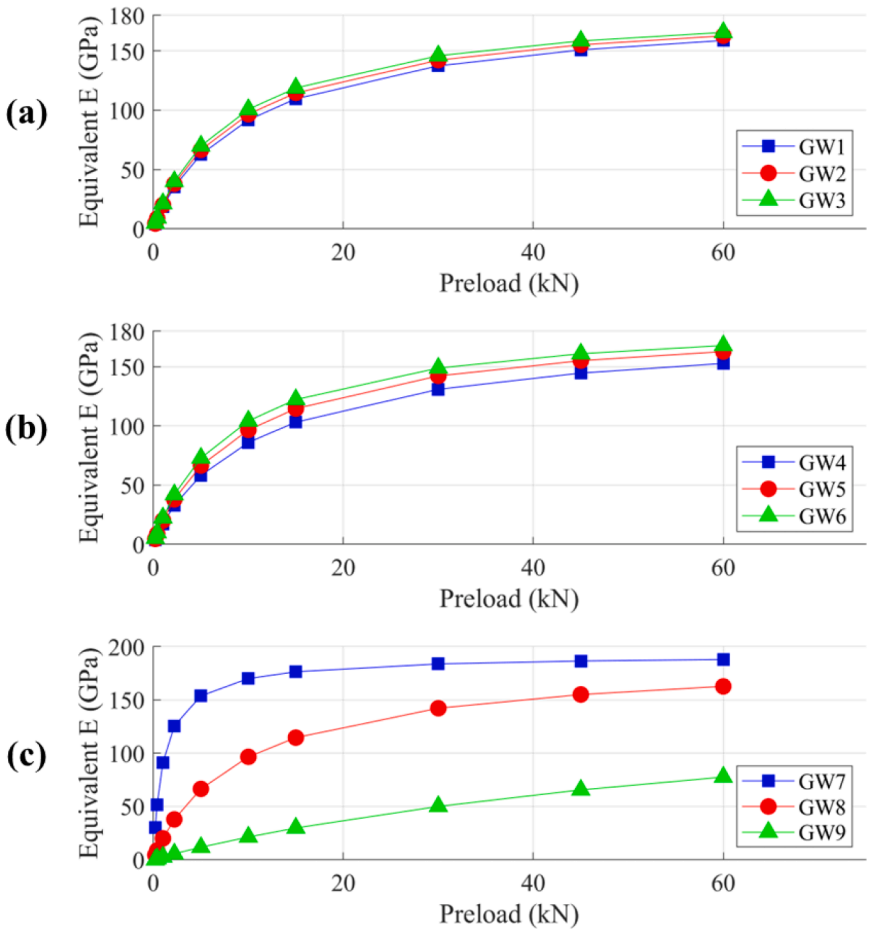

Fig. 8. $E_{coupling}$ vs. preload with various GW parameters, for (a) increasing R_s, (b) increasing η_s, and (c) increasing σ_s.

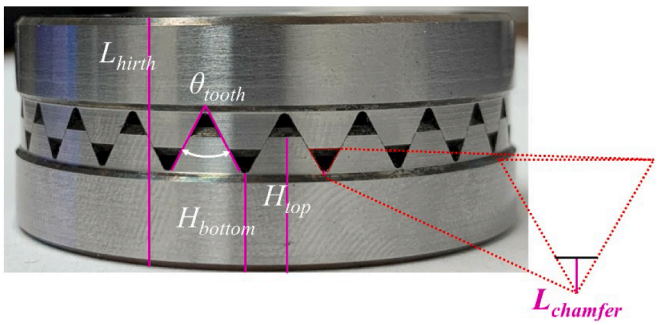

Fig. 9. Hirth coupling viewed from the side [19].

4.3. $\Phi_{coupling}$: equivalent transverse shear effect

The bending stiffness is influenced by the interaction between the tooth characteristics and the applied preload. Fig. 9 shows a side view of the Hirth coupling used for the case study obtaining the equivalent beam. Table 4 shows the Hirth coupling parameters. A comprehensive approach for modeling the Hirth coupling in three dimensions is provided in reference [19].

Fig. 10(a) shows the 3D solid element elastic Hirth coupling model connected between two 3D solid element rigid shafts, and (b) shows the equivalent beam for the Hirth coupling, connected between two beam element rigid shafts. Fig. 10(c) shows the von Mises stress plot of the Hirth coupling with the application of a 90 kN axial preload. The parameters and values for the Hirth coupling are provided in [19]. Table 5 lists the material properties and geometries for the assembly. A preload is applied on each end as shown. The

Table 4
Hirth coupling parameters [19].

Symbols	Definitions	Values
r_{out}	outer radius	24.5 mm
r_{in}	inner radius	10 mm
N_t	number of teeth	24
θ_{tooth}	tooth angle	60°
L_{hirth}	Hirth coupling thickness	20.55 mm
H_{bottom}	distance from base to dedendum	7.7 mm
H_{top}	distance from base to addendum	11.2 mm
$L_{chamfer}$	chamfer length	0.2 mm

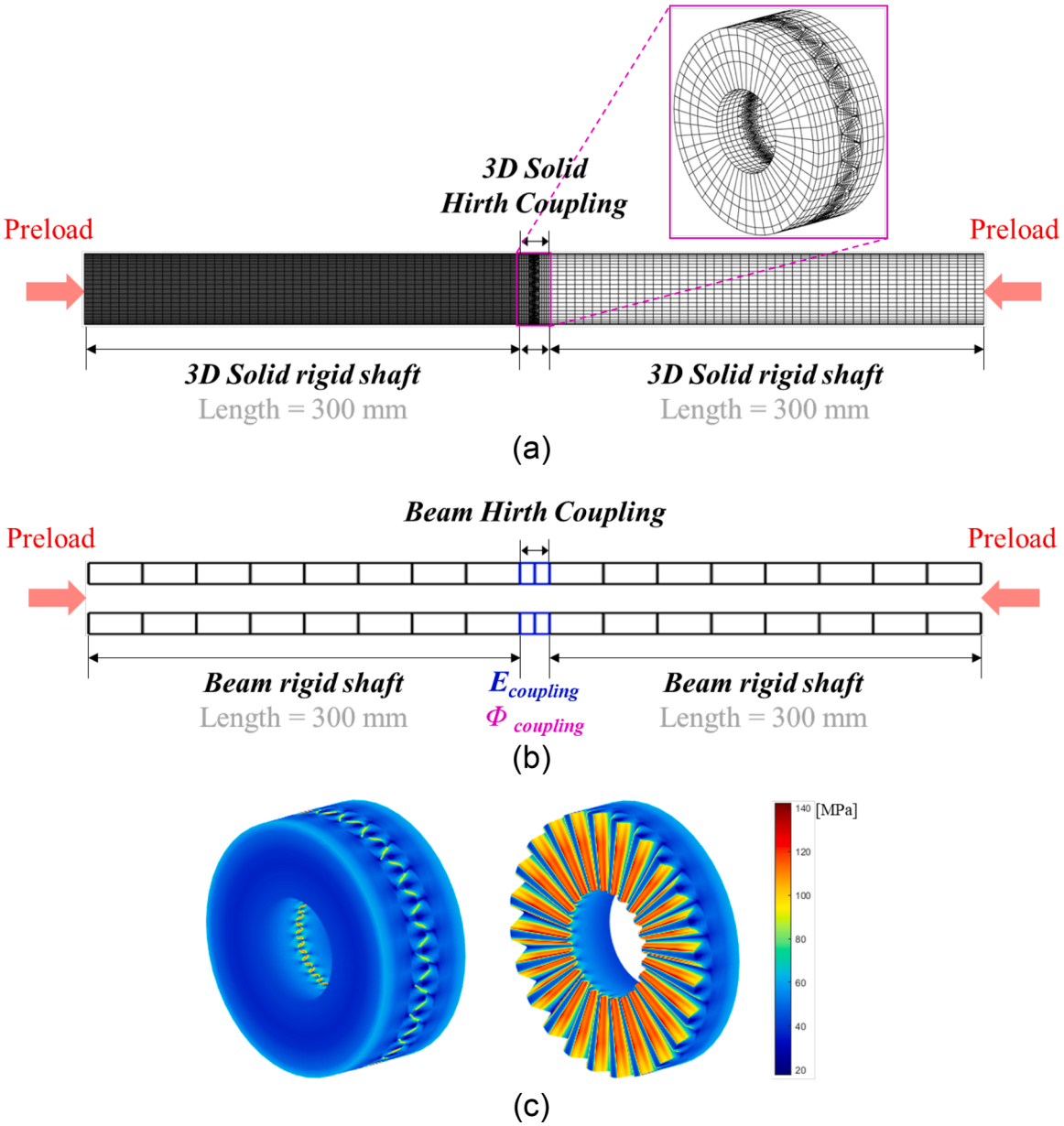

Fig. 10. Converged mesh of rigid shaft and elastic Hirth coupling assembly; (a) 3D solid element model, (b) Beam element model, and (c) von Mises stress of the Hirth coupling with axial preload of 90 kN.

Table 5
Properties of the rigid shaft and elastic Hirth coupling assembly [19].

	OD [mm]	ID [mm]	L [mm]	ρ [kg/m^3]	E [GPa]	ν
Shaft	49	20	300	8523	5000	0.3
Hirth coupling	49	20	20.55	8295	210	0.3

Table 6
Measured composite GW parameters between the shaft and Hirth coupling [19].

	Composite GW contact parameters		
Connection	R_s [m]	η_s [1/m^2]	σ_s [m]
Shaft - Hirth base	10.738E-06	1.882E+10	0.3189E-06
Hirth tooth - tooth	8.093E-06	1.721E+10	0.7031E-06

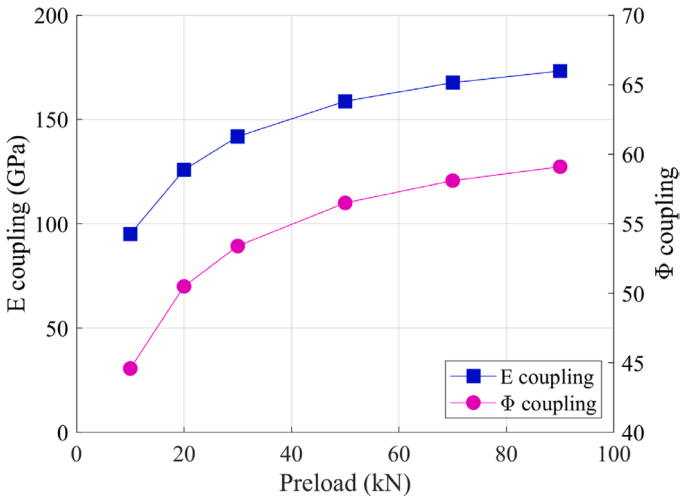

Fig. 11. $E_{coupling}$ and $\Phi_{coupling}$ vs. preload for the Hirth coupling contact.

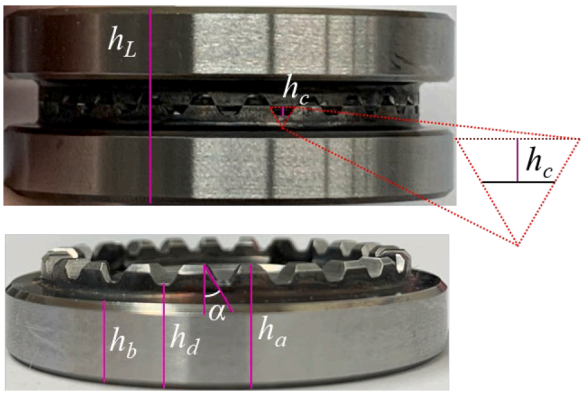

Fig. 12. Side views of the assembled and separated Curvic coupling [4].

same method illustrated in the previous section is utilized to obtain $E_{coupling}$ of the Hirth coupling.

The second natural frequencies were also experimentally measured along with the first natural frequencies in [19]. Eq. (11) shows that the Timoshenko beam element includes a transverse shear effect Φ to account for shear deformation. The second mode shape shows a large shear motion near the coupling when the shafts connected to the coupling are treated as rigid. The lower $E_{coupling}$ lowers the shear modulus G, which helps to lower the second bending natural frequency, improving agreement between the 3D solid and beam element models. The agreement may be further improved by defining an equivalent transverse shear effect $\Phi_{coupling}$, adjusted to

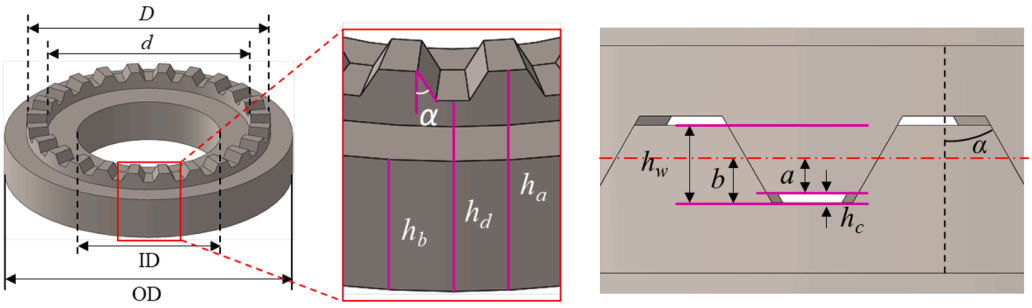

Fig. 13. Curvic coupling profile parameters viewed from the side and radial direction [4].

Table 7
Curvic coupling parameters [4].

Categories	Symbols	Definitions	Values	Geometric constraint
Independent parameters	OD	Base outer diameter	50.8 mm	
	ID	Base inner diameter	25.4 mm	
	D	Curvic tooth outer diameter	43 mm	$R = 21.5\ mm$
	d	Curvic tooth inner diameter	36 mm	$r = 18\ mm$
	N_t	Number of teeth	24	Even number
	N_x	Half pitch number	21	$N = 2n+1,$ $n \in [0,\ Z-1]$
	α	Pressure angle	30 °	
	h_a	Height of addendum	10.7 mm	
	h_d	Height of dedendum	9.0 mm	
	h_b	Height of base	7.5 mm	
	h_c	Clearance	0.3 mm	
Dependent parameters	β	Angle between r_m and S	78.75 °	$\beta = 90°\frac{N_x}{N_t}$
	W	Tooth width	3.5 mm	$W = \frac{D-d}{2}$
	r_m	Mean radius of Curvic Coupling	19.75 mm	$r_m = 0.5\left(\frac{D}{2}+\frac{d}{2}\right)$
	r_w	Grinding wheel radius	99.29 mm	$r_w = r_m\tan\beta$
	S	Wheel distance	101.235 mm	$S = \frac{r_m}{\cos\beta}$
	h_w	Whole depth	1.7 mm	$h_w = h_a - h_d$ $h_w = a+b$
	a	Addendum	0.7 mm	$a = \frac{h_w - h_c}{2}$
	b	Dedendum	1 mm	$b = a+h_c$
	h_e	Chamfer length	1.44 mm	$h_e = h_d - h_p + \frac{x_c}{\tan(\alpha)}$

lessen the difference in the second natural frequencies. The equivalent transverse shear effect $\Phi_{coupling}$ for the coupling is obtained after, and in the same manner, as $E_{coupling}$. The transverse shear effect Φ of the beam Hirth coupling, shown in Fig. 10(b), is varied so that the second bending natural frequency of the beam rigid shafts–beam Hirth coupling with $E_{coupling}$ and $\Phi_{coupling}$ model, matches that of the 3D solid element rigid shafts–3D solid element Hirth coupling model. The parameter $\Phi_{coupling}$ improves accuracy of the second natural frequency, while having little influence on the first natural frequency. Fig. 10 shows that there are three contact interfaces but only two different sets of GW parameters are required for the Hirth coupling because the composite surface roughness of first and third contact are the same. The measured GW parameters of the contact surface roughness related to the Hirth coupling are listed in Table 6. By conducting ten measurements of the surface roughness on the Hirth coupling and shaft contact face, the relative standard uncertainty of the parameter σ_s is determined to be within the range of 7–13% [19]. Fig. 11 shows $E_{coupling}$ and $\Phi_{coupling}$ versus preload for the Hirth coupling. The result shows that both $E_{coupling}$ and $\Phi_{coupling}$ increase with the increase of preload.

$E_{coupling}$ and $\Phi_{coupling}$ for a Curvic coupling are obtained in the same manner as for the Hirth coupling. Fig. 12 shows a side view of the Curvic coupling used for the case study obtaining the equivalent beam. Fig. 13 and Table 7 illustrates the Curvic coupling parameters and corresponding values. A comprehensive approach for modeling the Curvic coupling in three dimensions is provided in reference [4].

Fig. 14(a) shows a 3D solid Curvic coupling model connected by two 3D solid element rigid shafts. Fig. 14(c) shows the von Mises stress plot of the Curvic coupling with the application of a 70 kN axial preload. The parameters and corresponding values for the 3D Curvic coupling are provided in [4]. Table 8 lists the measured GW parameters for the three contact faces. The relative standard deviation of the parameters σ_s for ten measurements was calculated and it ranged between 6 and 12%.

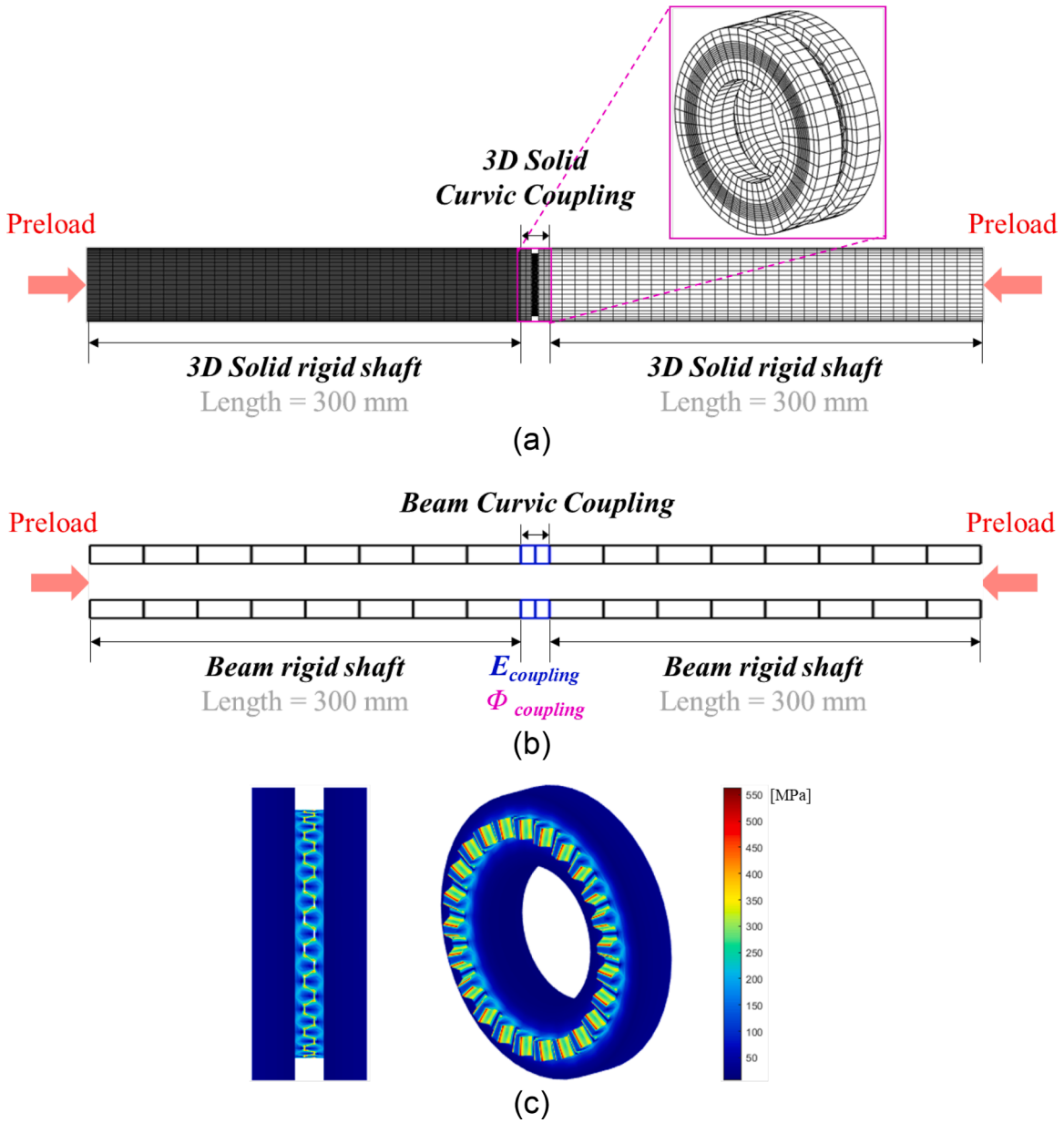

Fig. 14. Converged mesh of the rigid shaft and elastic Curvic coupling assembly; (a) 3D solid element model, (b) Beam element model, and (c) von Mises stress of the Curvic coupling with axial preload of 70 kN.

Table 8
Measured composite GW parameters for the shaft and the Curvic coupling [4].

	Composite GW contact parameters		
Connection	R_s [m]	η_s [1/m^2]	σ_s [m]
Shaft - Curvic bottom	1.171E-06	10.429E+10	3.431E-06
Curvic tooth - Curvic tooth	6.087E-06	2.770E+10	0.2458E-06

Fig. 15 shows the increase of both $E_{coupling}$ and $\Phi_{coupling}$ with axial preload for the Curvic coupling. The asymptotic value of $E_{coupling}$ is approximately 80 GPa which is less than the actual E value for steel, 200 GPa. One may expect the coupling to behave similar to a continuous beam for extremely high preload values. This is the case here when one considers the area moments of inertia of the solid element and beam element models for the toothed section. The EI product of the high preload beam and solid models are in close

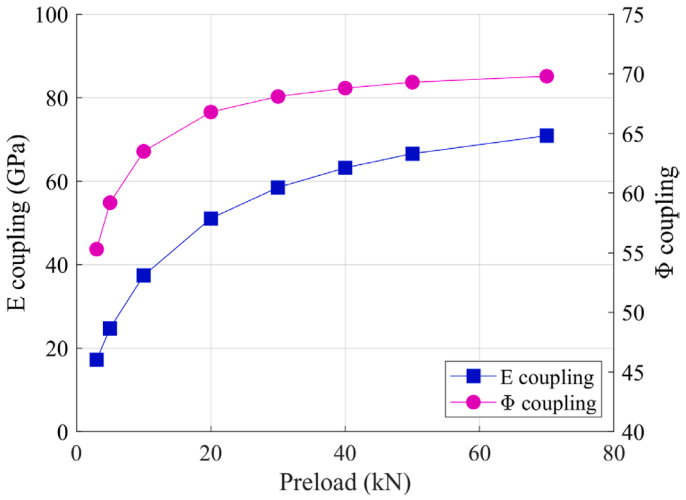

Fig. 15. $E_{coupling}$ and $\Phi_{coupling}$ vs. preload for the Curvic coupling beam model.

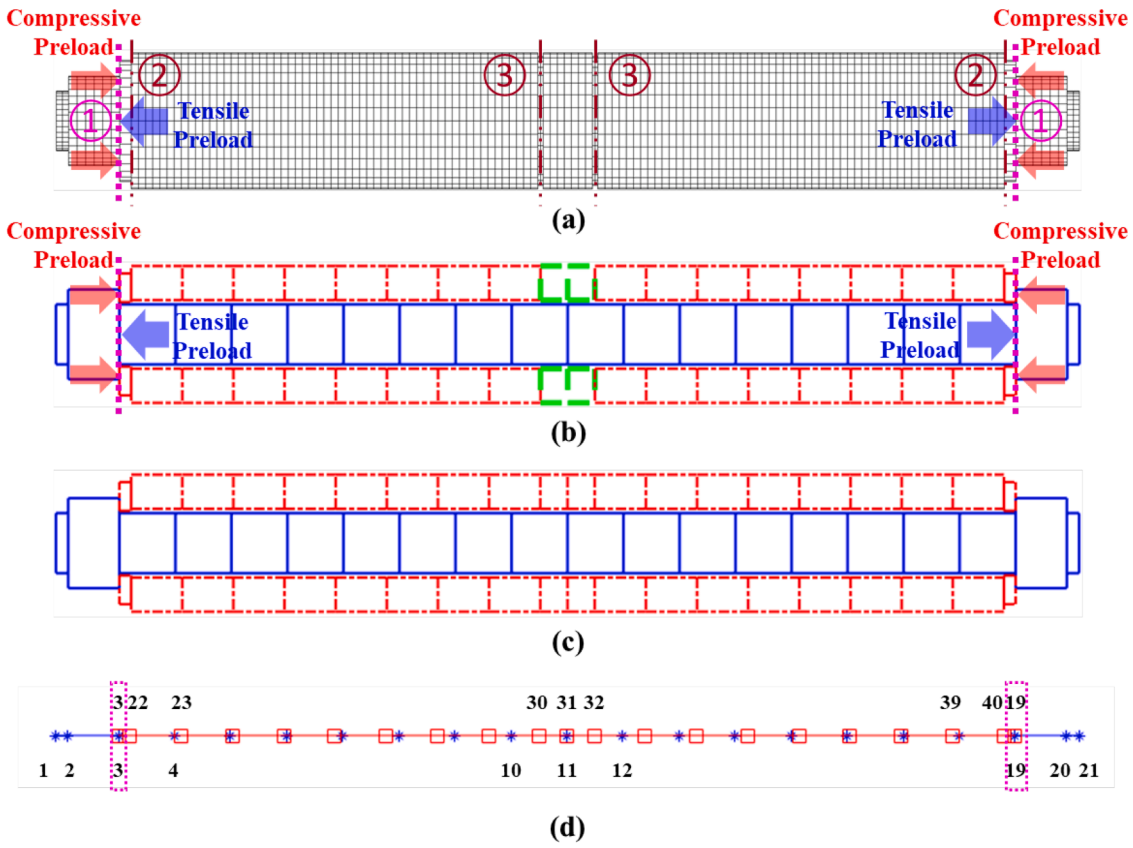

Fig. 16. Test rotor assembly with butt joint (a) converged 3D solid element mesh, (b) equivalent beam element mesh, (c) Timoshenko beam element mesh, and (d) beam element in 1D form.

Table 9
Properties of the test rotor assembly with the butt joint [18].

	OD (mm)	ID (mm)	L (mm)	ρ (kg/m^3)	E (GPa)	ν
Through- bolt	22.23	0	381.00	7837	205	0.3
Nut	33.34	22.23	19.05	8202	205	0.3
Washer	45.21	24.00	4.32	7929	205	0.3
Outer annular shaft	50.8	25.4	152.4	8202	205	0.3
Center butt joint	50.8	25.4	20.32	8202	205	0.3

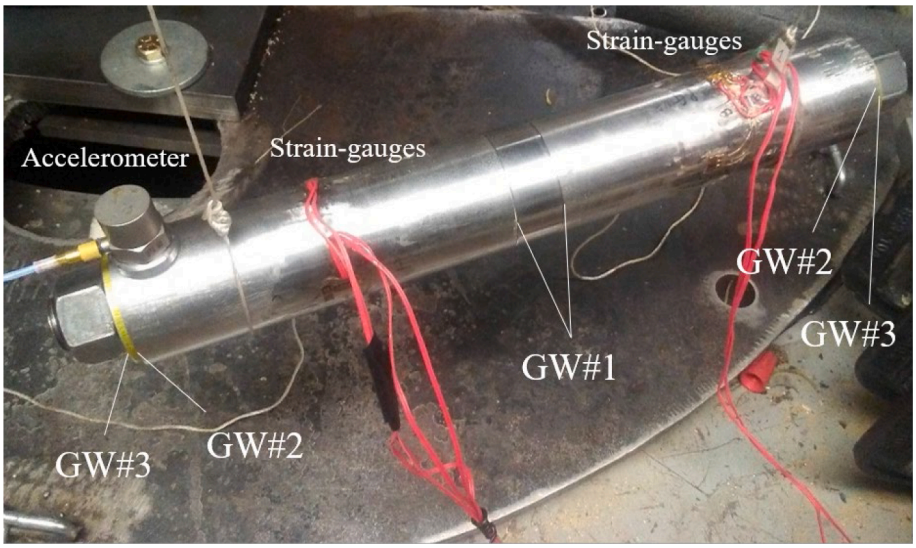

Fig. 17. Test rotor assembly with the butt joint [18].

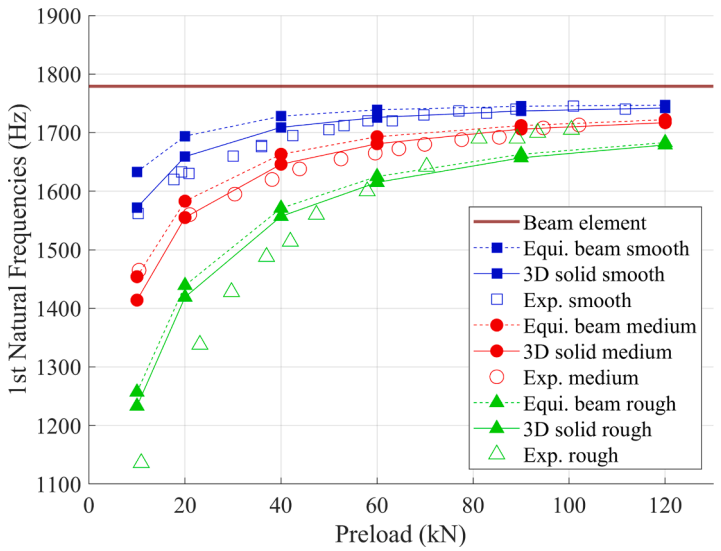

Fig. 18. Measured and predicted bending mode natural frequencies of 3D solid element, equivalent beam element, and Timoshenko beam element models of the test rotor with butt joint.

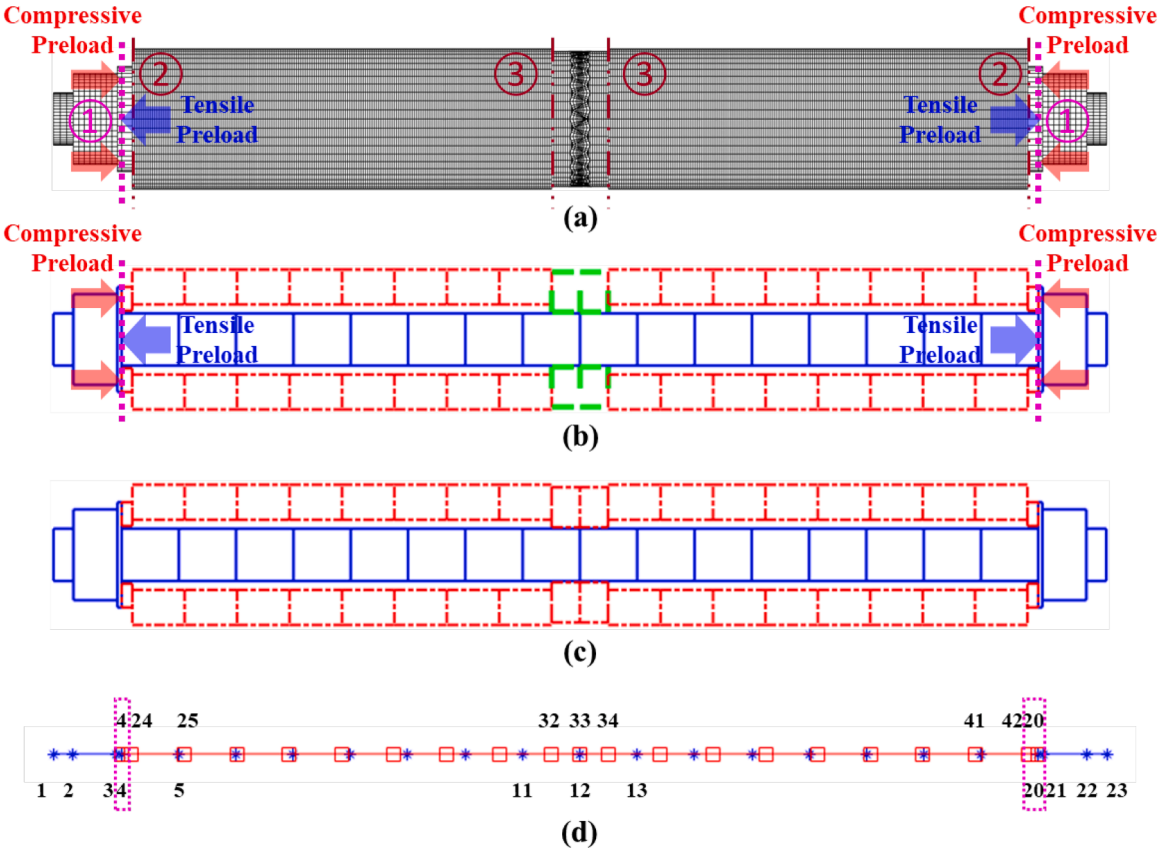

Fig. 19. Test rotor assembly with the Hirth coupling (a) converged 3D solid element mesh, (b) equivalent beam element mesh, (c) Timoshenko beam element mesh, and (d) beam element in 1D form.

agreement as preload is increased to the asymptotic limit. A final point is that commercial beam based rotordynamic codes may not have an input for specifying Φ but typically will have one for the shear form factor k, which is readily obtained from Φ in Eq. (11).

5. Verification of various axial contact models

5.1. Test rig with butt joint

The primary objective of obtaining $E_{coupling}$ and $\Phi_{coupling}$ based on detailed 3D solid element modeling is to accurately represent the coupling in commercially available beam based rotordynamic simulation software. The converged mesh, beam and 3D solid element models with the butt joint [18] are shown in Fig. 16. The corresponding material properties are shown in Table 9. Fig. 16(a) shows the 3D solid element mesh and Fig. 16(b), (c) and (d) depict the beam model. The thick green dashed line mesh at the center of the rotor in Fig. 12(b) represents the butt joint beam element with $E_{coupling}$. Fig. 16(c) shows the Timoshenko beam model and Fig. 16(d) shows its 1D form. Fig. 17 shows the test rotor assembly with the butt joint.

There are two distinct sub-assemblies defined: the outer member sub-assembly (OMA) and the inner member sub-assembly (IMA). The OMA consists of two washers, two shafts, and a butt joint. They are represented in red dash-dotted lines and thick green dashed lines in Fig. 16(b). The corresponding nodes for the OMA in Fig. 16(d) are from nodes 22 to 40, node 3, and node 19. The IMA consists of the through-bolt and two nuts represented as the blue solid line mesh. The corresponding node numbers for the IMA in Fig. 16(d) are from node 1 to 21. Note that node number 3 and 19 are shared by both sub-assemblies. The two assemblies are connected in parallel where the pressure boundaries are applied. The pressure boundary faces for the test rotor are highlighted by pink dotted lines in Fig. 16 (a) and (b) and are marked as face 1. Torque was applied to the through-bolt and nuts to provide axial preload on the shafts [35]. This results in the through-bolt and nuts being in tension, while the washers, shafts, and butt joint are in compression.

Fig. 18 shows a comparison between the measured and predicted free-free bending mode natural frequencies of the 3D solid element model, equivalent beam model, and the Timoshenko beam model for the test rotor with the butt joint. The measured and predicted natural frequencies for the 3D solid element model and equivalent beam model with different surface roughness all agree very well. The free-free bending mode natural frequency for the uniform Timoshenko beam model without preload is 1779 Hz, which is significantly higher than all measured data especially at low preloads and with a rough surface finish at the butt joint.

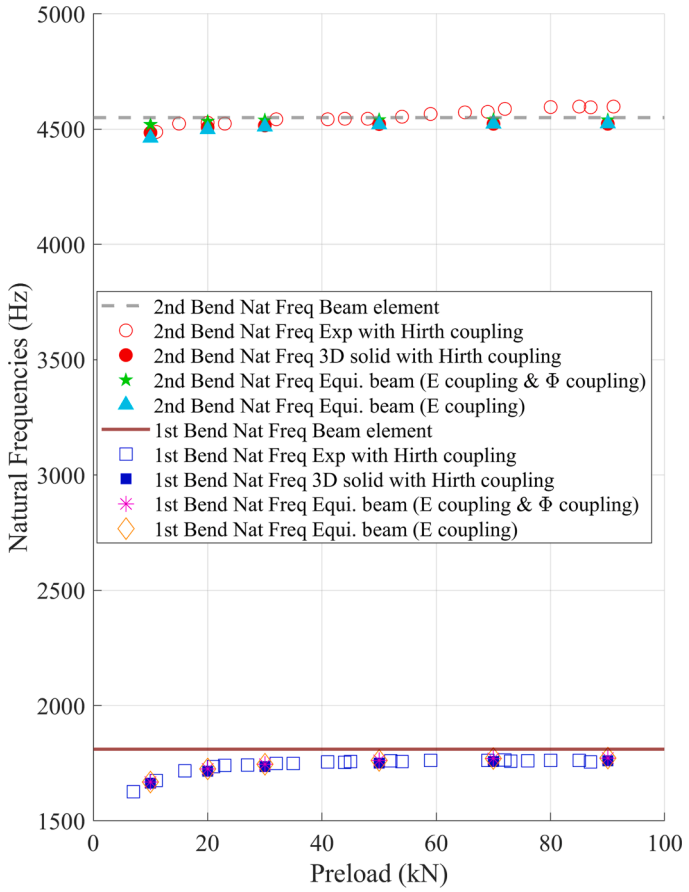

Fig. 20. Measured and predicted bending mode natural frequencies of the 3D solid element, equivalent beam element, and Timoshenko beam models for the test rotor with a Hirth coupling.

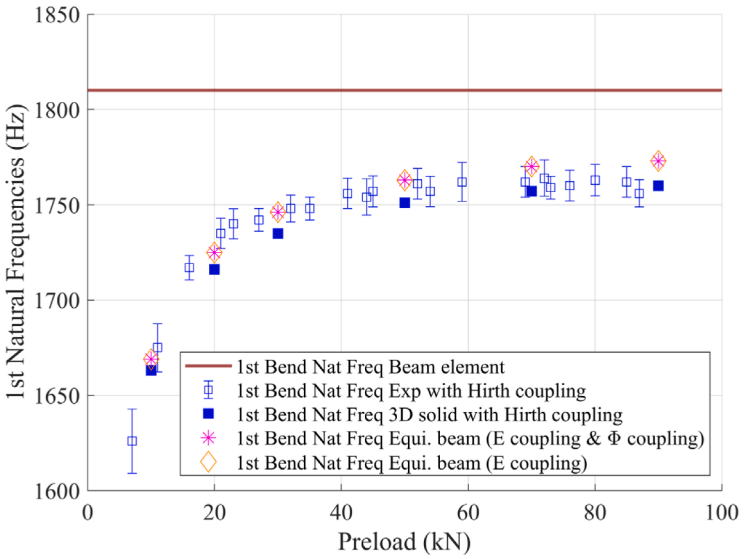

Fig. 21. Measured and predicted first bending mode natural frequencies of the 3D solid element, equivalent beam element, and Timoshenko beam models for the test rotor with a Hirth coupling.

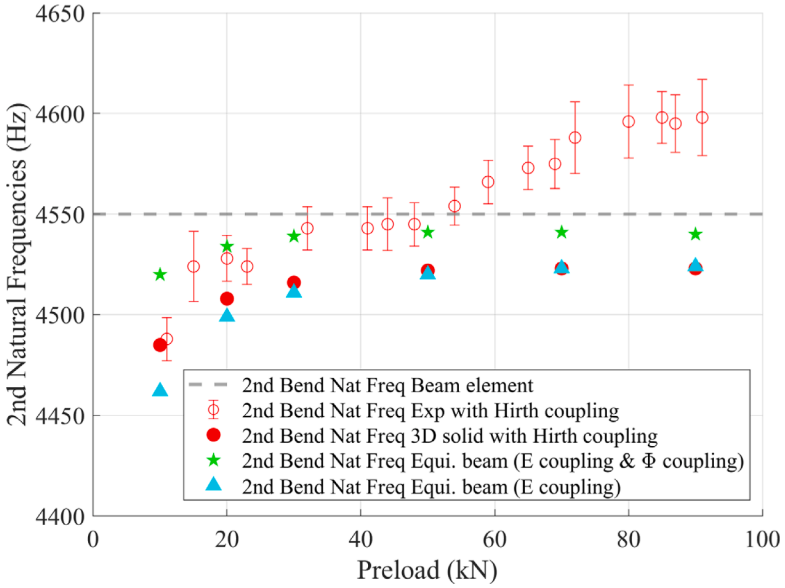

Fig. 22. Measured and predicted second bending mode natural frequencies of the 3D solid element, equivalent beam element, and Timoshenko beam models for the test rotor with a Hirth coupling.

In a design stage scenario, the measured data is generally unavailable however the solid element model results may be available. Thus, it is practical to compare the beam predictions with the 3D solid element predictions, especially when considering the good correlation of the solid element model with measured data in Fig. 18. The maximum difference between the prediction of the 3D solid element model and the Timoshenko beam model is about 546 Hz at the preload of 10 kN with rough surface, which is a 44.3% error. This error is significantly reduced by using the equivalent beam element $E_{coupling}$ for the butt joint model. In this case the beam prediction model is only 24 Hz higher than the solid element model prediction at 10 kN preload and with the rough surface. This reduces the error of the beam mode prediction from 44.3% to 1.9%. Similarly, the maximum difference between the equivalent beam and the 3D solid element model predictions is 61 Hz at a preload of 10 kN with a smooth surface, which is a 3.9% error. The predictions of the equivalent beam model are closely aligned with the 3D solid element model with contact effect prediction for all surface roughness, and preloads. The equivalent beam model performs exceptionally well for all surface roughness. The pressure resulting from the preload can be determined through contact area calculations by utilizing the diameter information provided in Table 9. Dividing this pressure by the yield strength of the steel, which is 450 MPa, allows for the normalization of the preload. The corresponding normalized preloads for values of 10, 20, 40, 60, 90, and 120 kN are 0.053, 0.106, 0.211, 0.317, 0.476, and 0.634, respectively.

5.2. *Test rig with Hirth coupling*

Fig. 19 shows the converged mesh 3D solid and Timoshenko beam element geometries for the prediction models with the Hirth coupling [19]. Appendix B includes Fig. B.1 depicting the test rotor assembly with the Hirth coupling, and the properties of the test rotor assembly are listed in Table B.1 [19]. The thick green dashed line mesh at the center of the rotor in Fig. 19(b) represents the Hirth coupling that has properties of $E_{coupling}$ and $\Phi_{coupling}$ from Fig. 11. Fig. 19(c) and (d) show the Timoshenko beam model and a 1D representation with node numbers, respectively. Fig. 19(a) shows the seven contact interfaces. Pink dotted lines indicate the pressure boundary faces for the test rotor among the contact interfaces. The OMA and IMA of the beam model share the pressure boundary nodes, which are node 4 and 20 in Fig. 19(d). Fig. 20 shows the measured and predicted free-free first and second bending mode natural frequencies of the 3D solid element model, equivalent beam model, and the Timoshenko beam model for the test rotor with the Hirth coupling. The natural frequencies of the rotor are predicted with preloads of 10, 20, 30, 50, 70, and 90 kN. Figs. 21 and 22 show zoom views of the 1st and 2nd bending mode natural frequencies, respectively. The first mode measured and predicted natural frequencies for the 3D solid model and equivalent beam model agree well, and $\Phi_{coupling}$ has little effect on the beam model first natural frequency. The second natural frequency prediction of the equivalent beam model with $E_{coupling}$ and $\Phi_{coupling}$ has better accuracy than with only $E_{coupling}$. The free-free first and second bending mode natural frequencies for the Timoshenko beam model without preload are 1810 Hz and 4550 Hz, respectively. The first natural frequency difference between the 3D solid model with Hirth coupling and the Timoshenko beam is 147 Hz at a preload of 10 kN, while the difference between the 3D solid Hirth coupling and equivalent beam is only 6 Hz at the same preload. By dividing the pressure by the yield strength of the material, the normalized preloads for values of 10, 20, 30, 50, 70, and 90 kN are determined to be 0.028, 0.056, 0.084, 0.140, 0.195, and 0.251, respectively. These findings indicate that the natural frequency of the system equipped with the Hirth coupling tends to approach the upper limit at lower normalized preload levels.

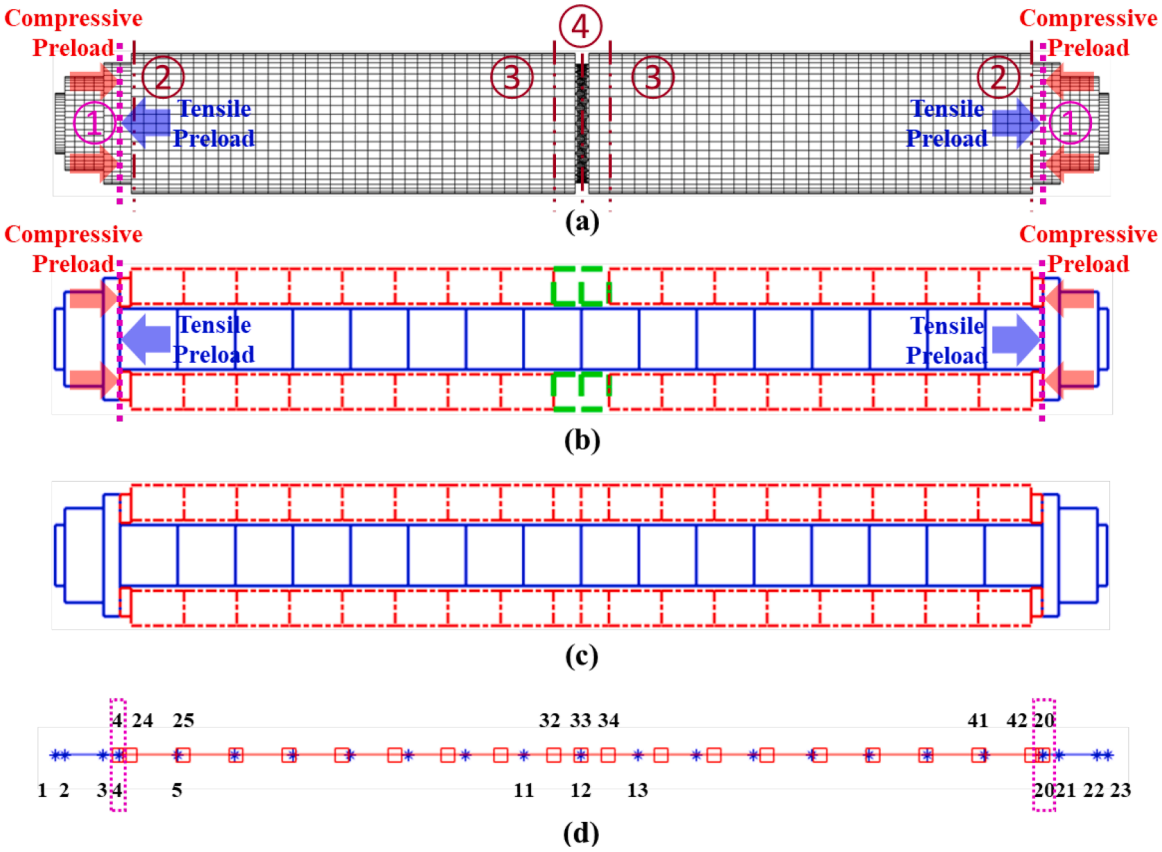

Fig. 23. Test rotor assembly with the Curvic coupling (a) converged 3D solid element mesh, (b) equivalent beam element mesh, (c) Timoshenko beam element mesh, and (d) beam element in 1D form.

5.3. *Experiment – theory comparison for curvic coupling*

Fig. 25 shows the geometry of the prediction models for 3D solid elements including the Curvic coupling [4], and for beam elements with a converged mesh. Appendix B includes Fig. B.2 depicting the test rotor assembly with the Curvic coupling, and the properties of the test rotor assembly are listed in Table B.2 [4]. The thick green dashed line mesh at the center of the rotor in Fig. 23(b) represents the beam elements with $E_{coupling}$ and $\Phi_{coupling}$ from Fig. 15, which represents the 3D solid Curvic coupling. Fig. 23(c) and (d) show the Timoshenko beam model mesh and a 1D model representation with node numbers, respectively. The pressure boundary faces for the test rotor are indicated by pink dotted lines in Fig. 23(a) and (b). The pressure boundary nodes shared by the OMA and IMA of the beam model are nodes 4 and 20 in Fig. 23(d).

The efficacy of the equivalent $E_{coupling}$ and $\Phi_{coupling}$ approach was investigated by comparison with the solid element model and measured natural frequencies. Fig. 24 shows the measured and predicted free-free first and second bending mode natural frequencies of the 3D solid element model, equivalent beam model, and the uniform Timoshenko beam model for the test rotor, with a Curvic coupling. Figs. 25 and 26 show zoomed-in views of the first and second bending mode natural frequencies, respectively.

The measured and predicted natural frequencies for the 3D solid element and equivalent beam models agree well for both first and second bending mode natural frequencies. Free-free first and second bending mode natural frequencies for the Timoshenko beam model without preload are 1774 Hz and 4454 Hz, respectively, which are far from the values predicted by the high fidelity solid element model. Use of the equivalent beam approach significantly narrows the gap between the solid element and beam model predictions. The maximum difference between the 3D solid element model with Curvic coupling, and the Timoshenko beam model is 629 Hz at a preload of 3 kN, yielding a 55% difference. In comparison, the maximum difference between the 3D solid element model with Curvic coupling and the equivalent beam model is only 18 Hz at the same preload. The relative error decreases from 55% to 1.5% for this example. The predicted natural frequencies of the equivalent beam model are always located between those of the Timoshenko beam and the 3D solid element models. The normalized preloads, that are obtained by dividing the pressure by the yield strength of the material for preloads of 3, 5, 10, 20, 30, 40, 50, and 70 kN, are 0.004, 0.007, 0.014, 0.029, 0.043, 0.057, 0.071, and 0.100. Fig. 27 shows the free-free first and second bending mode shapes prediction for the equivalent beam model for the test rotor with the Curvic coupling at a preload of 70 kN. The red dotted line represents the OMA modal deflection, and the blue solid line indicates the IMA modal deflection.

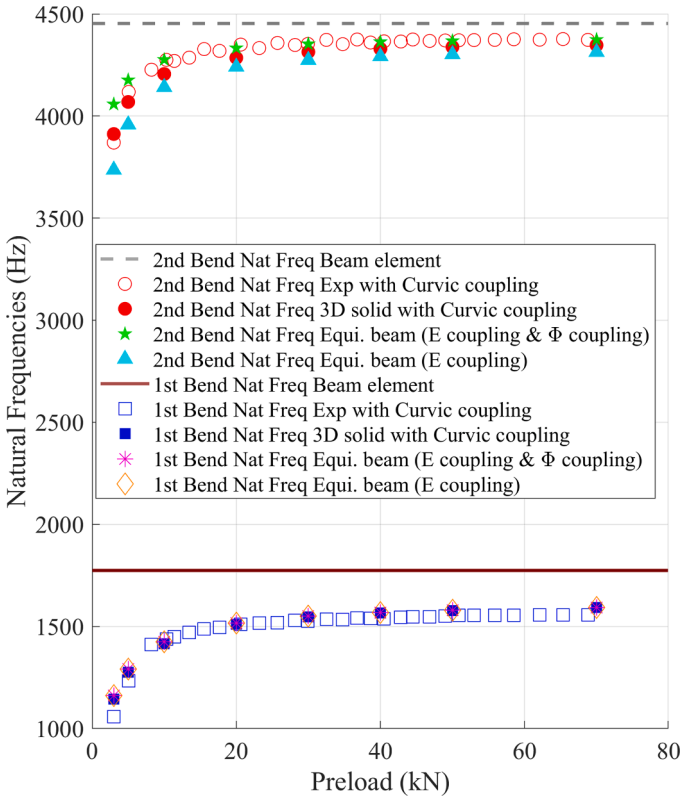

Fig. 24. Measured and predicted bending mode natural frequencies of the 3D solid element, equivalent beam, and uniform Timoshenko beam models for the test rotor with a Curvic coupling.

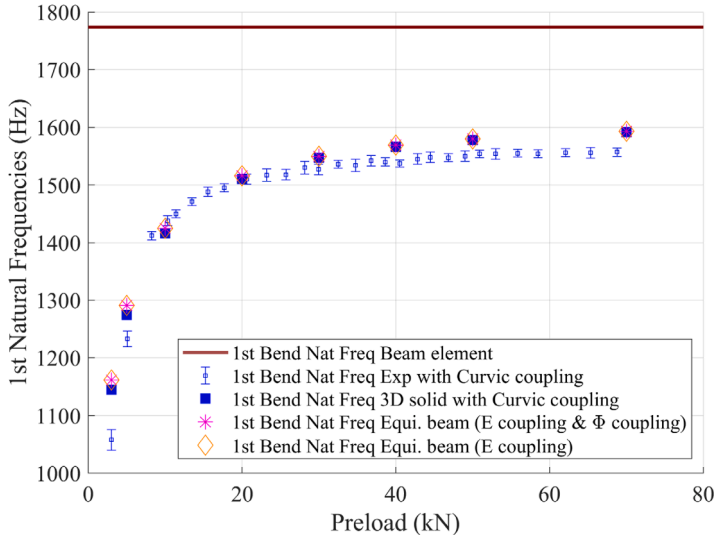

Fig. 25. Measured and predicted first bending mode natural frequencies of the 3D solid element, equivalent beam, and uniform Timoshenko beam models for the test rotor with a Curvic coupling.

6. Example: overhung rotor-bearing system model

6.1. de Jongh rotor with equivalent beam model

The preceding sections discussed test and theoretical results for a novel modeling approach utilizing an equivalent beam model for

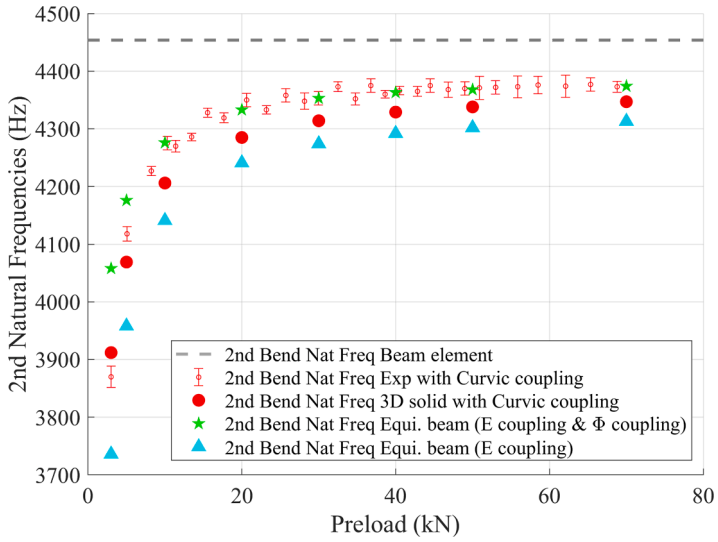

Fig. 26. Measured and predicted second bending mode natural frequencies of the 3D solid element, equivalent beam, and uniform Timoshenko beam models for the test rotor with a Curvic coupling.

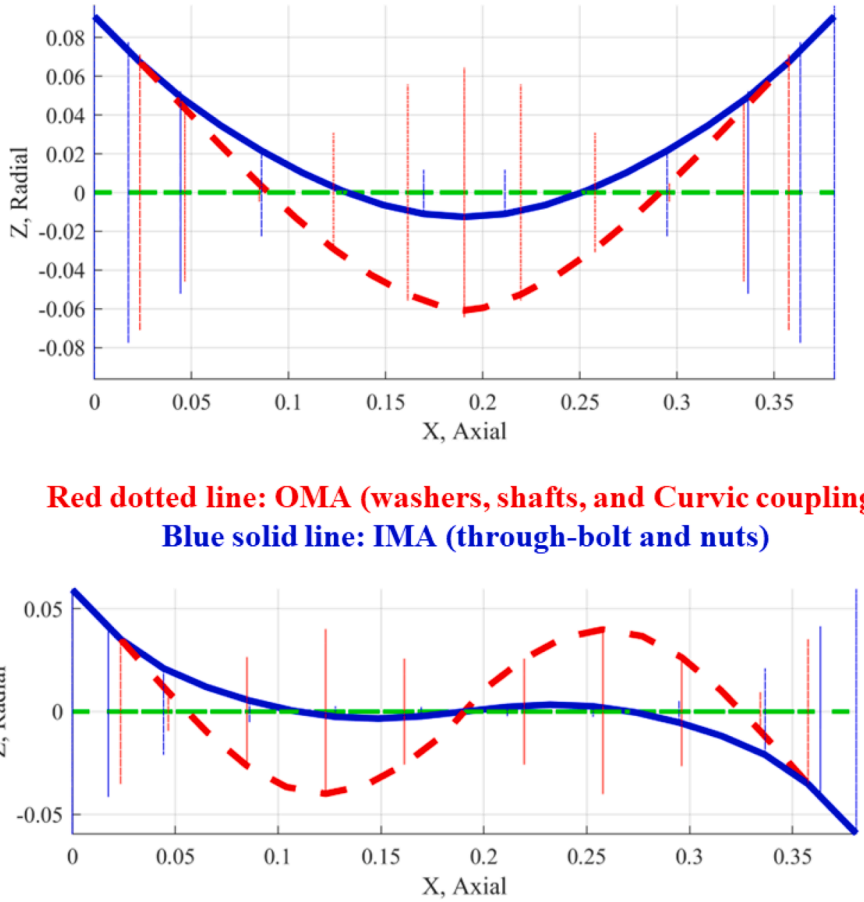

Fig. 27. Predicted free-free first and second bending mode shapes of the equivalent beam model for the test rotor with a Curvic coupling at a preload of 70 kN.

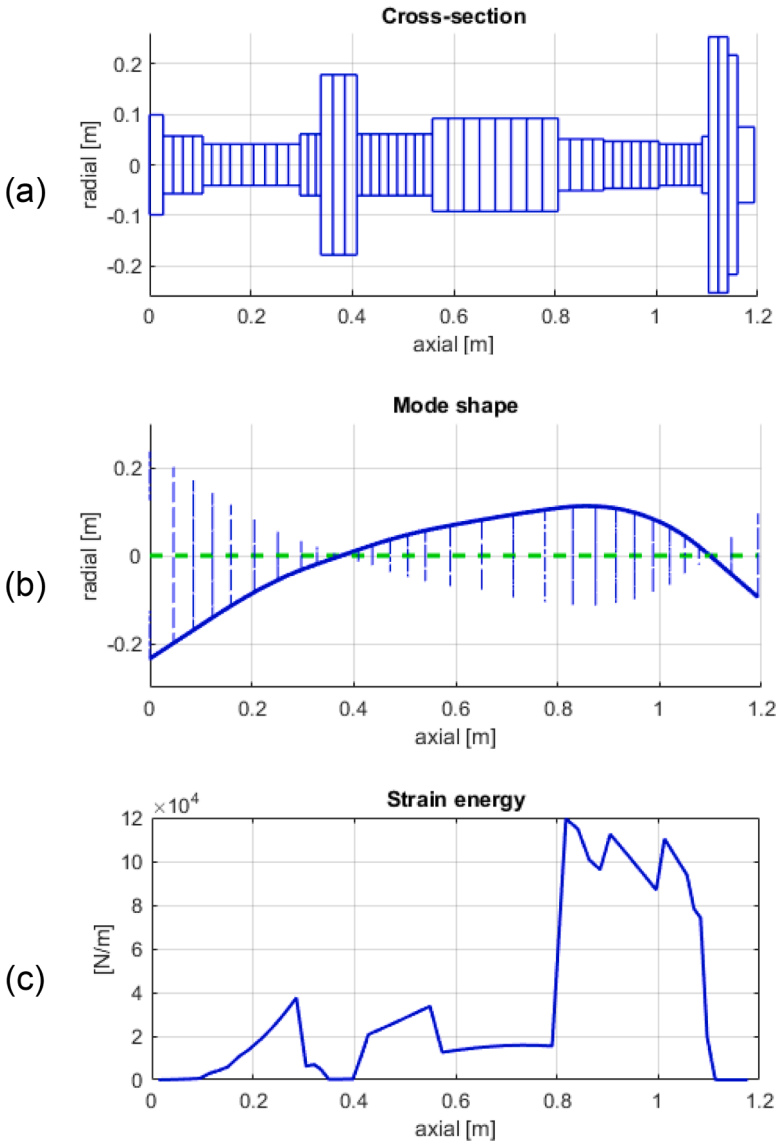

Fig. 28. Overhung-type de Jong rotor; (a) beam model cross section, (b) free-free first bending mode and (c) corresponding strain energy along the axial direction.

a butt joint, and Hirth, or Curvic couplings. The approach was demonstrated with a short non-rotating, preloaded shaft. In this section, the effectiveness of the equivalent beam model approach is demonstrated for an industrial class rotor model. The overhung-type de Jongh rotor was presented and analyzed in detail in [36,37]. Fig. 28 shows the cross section, free-free first bending mode, and internal strain energy due to the modal deflection along the axial direction of the overhung de Jongh rotor beam model. The Young's modulus of the beams is 200 GPa and the density is 7850 kg/m^3. The simulated free-free first bending mode natural frequency of the beam model is 200 Hz. The internal elemental strain energy U_{md} is determined from the modal deformation $\underline{q_{modal}}$ and the beam element stiffness matrix $\underline{\boldsymbol{K}_{be}}$.

$$U_{md} = \frac{1}{2}\underline{\boldsymbol{q}_{modal}}^{\mathrm{T}}\ \underline{\boldsymbol{K}_{be}}\ \underline{\boldsymbol{q}_{modal}} \tag{38}$$

The maximum bending occurs where the strain energy is maximum (0.82 m). The rotating assembly of de Jongh rotor is modified to investigate the effectiveness of the equivalent beam model by comparing it with the 3D solid element model with contact effect. Fig. 29 shows the three 3D solid element models of the de Jongh rotor with a butt joint, Hirth coupling, and Curvic coupling located near the maximum bending point. The models also consist of other components such as a through-bolt, the shaft, and an overhung impeller. The inner and outer diameters of the butt joint, Hirth coupling, and Curvic couplings are 102 mm and 42 mm, respectively. The other parameters for the Hirth coupling and Curvic coupling are listed in Table 10 and Table 11, respectively.

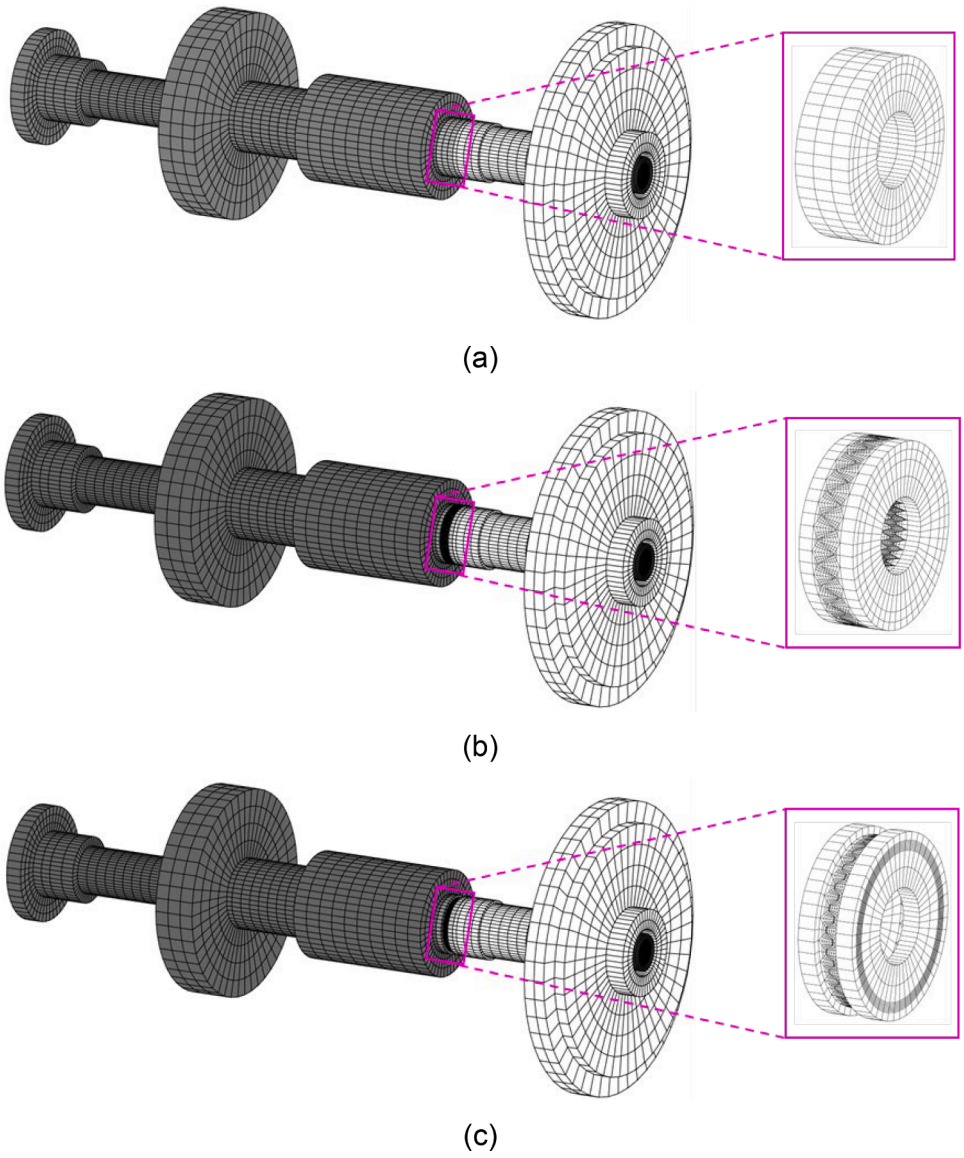

Fig. 29. Three distinct 3D solid models of a de Jongh rotor with (a) butt joint, (b) Hirth coupling, and (c) Curvic coupling.

Table 10
Hirth coupling parameters located at $x = 0.82$ m of de Jongh model.

Symbols	Definitions	Values
r_{out}	outer radius	51 mm
r_{in}	inner radius	21 mm
N_t	number of teeth	24
θ_{tooth}	tooth angle	60°
L_{hirth}	Hirth coupling thickness	32.95 mm
H_{bottom}	distance from base to dedendum	11.5 mm
H_{top}	distance from base to addendum	19 mm
$L_{chamfer}$	chamfer length	0.8 mm

Fig. 30 shows the contact nodes at the interfaces. Clamping preload forces are applied on each end. The centrifugal force term $\underline{f}_c$ in Eq. (16) is incorporated due to rotor rotation. Guyan reduction is used to efficiently obtain the eigenvalues [38]. The GW parameters utilized in the case study are listed in Table 12. Use of the diameter of a wheel attached to the shaft as the shaft diameter in a beam model generally causes overly high bending stiffnesses and natural frequencies. To mitigate this error, wheels are modeled to only

Table 11
Curvic coupling parameters located at $x = 0.82$ m of de Jongh model.

Categories	Symbols	Definitions	Values	Geometric constraint
Independent parameters	OD	Base outer diameter	102 mm	
	ID	Base inner diameter	42 mm	
	D	Curvic teeth outer diameter	93 mm	
	d	Curvic teeth inner diameter	82 mm	
	N_t	Number of teeth	24	Even number
	N_x	Half pitch number	21	$N = 2n + 1$, $n \in [0,\ Z-1]$
	α	Pressure angle	30 °	
	h_a	Height of addendum	18 mm	
	h_d	Height of dedendum	14 mm	
	h_b	Height of base	10 mm	
	h_c	Clearance	1 mm	
Dependent parameters	β	–	78.75 °	$\beta = 90°\frac{N_x}{N_t}$
	W	Tooth width	5.5 mm	$W = \frac{D-d}{2}$
	r_m	Mean radius of Curvic Coupling	43.75 mm	$r_m = 0.5(\frac{D}{2} + \frac{d}{2})$
	r_w	Grinding wheel radius	219.95 mm	$r_w = r_m \tan\beta$
	S	Wheel distance	224.26 mm	$S = \frac{r_m}{\cos\beta}$
	h_w	Whole depth	4 mm	$h_w = h_a - h_d h_w = a + b$
	a	Addendum	1.5 mm	$a = \frac{h_w - h_c}{2}$
	b	Dedendum	2.5 mm	$b = a + h_c$

contribute lumped inertias to the model, and not stiffness. The predicted first natural frequency of the beam - lumped mass model shown in Fig. 31 is 198 Hz. Through-bolts are represented by blue beams, while shafts are represented by red beams. The green beams show the equivalent beams with $E_{coupling}$. The parameter $E_{coupling}$ is included to enhance the beam model of a butt, Hirth or Curvic coupling.

6.2. Natural frequencies of de Jongh rotor with the equivalent beam model

The calculated $E_{coupling}$ versus preload in relation to surface roughness is shown in Fig. 32(a). These values were determined as in the previous sections by adjusting the $E_{coupling}$ value in a beam model to match the solid element model results for a short rigid shaft model like shown in Fig. 6. Sigma1, Sigma2, and Sigma3 indicate the surface roughness in Table 12 with σ_s values varied as 1.0E-06, 2.0E-06, and 3.0E-06, respectively. Compared to Sigma2 and Sigma3, the surface roughness of Sigma1 is relatively smooth. The calculated $E_{coupling}$ vs. preload in relation to the coupling type is shown in Fig. 32(b). The same surface roughness (Sigma1) is used. It is found that the butt joint has a bigger $E_{coupling}$ than the Hirth or Curvic coupling.

The calculated $E_{coupling}$ from Fig. 32 is used in the green beam elements in Fig. 31 to determine the de Jongh rotor's first natural frequencies in relation to the surface roughness. The results are presented in Fig. 33. The natural frequencies of the rotor are predicted with preloads of 5, 10, 15, 30, 50, and 100 kN. The result demonstrates that the predicted natural frequencies for the 3D solid element model and equivalent beam model for de Jongh rotor agree well across a range of surface roughness.

The de Jongh rotor's first bending mode natural frequencies are shown in Fig. 34 for the 3 coupling types studied. Each assumes the same surface roughness (Sigma1). This demonstrates that the predicted natural frequencies for the 3D solid element and equivalent beam models agree well with the various coupling types.

6.3. Critical speeds of de Jongh rotor with equivalent beam model

Fig. 35 shows the stiffness and damping coefficients of the tilting pad journal bearings [39]. A rotor-fixed coordinate system is used to derive the equations of motion for the 3D solid element model of the rotor-bearing system. The bearing matrices in the inertial coordinate system are transformed into the rotor-fixed coordinate systems $\underline{\boldsymbol{K}}_{b,r}$ and $\underline{\boldsymbol{C}}_{b,r}$ as explained in [26].

Fig. 36 shows the predicted first critical speeds of the de Jongh rotor in relation to the surface roughness of the butt joint. The critical speeds of the Timoshenko beam model and continuous 3D solid single model are 6979 rpm and 6750 rpm, respectively. The equivalent beam model results show a significant improvement, relative to the Timoshenko beam, when benchmarking against the high fidelity solid element model with the rough surface at lower preload. For example, the relative error between the Timoshenko beam and the 3D solid butt joint model at a preload of 5 kN and Sigma3 surface roughness is 45%. The relative error between the equivalent beam model and the 3D solid butt joint model at the same preload and surface roughness is only 7%. The 3D solid model with contact effect approaches the continuous solid single model critical speed as the preload increases. In a similar way, the critical speed of the equivalent beam model approaches that of the Timoshenko beam model when the preload increases.

Fig. 37 shows the predicted first critical speeds of the de Jongh rotor in relation to the coupling type with the surface roughness

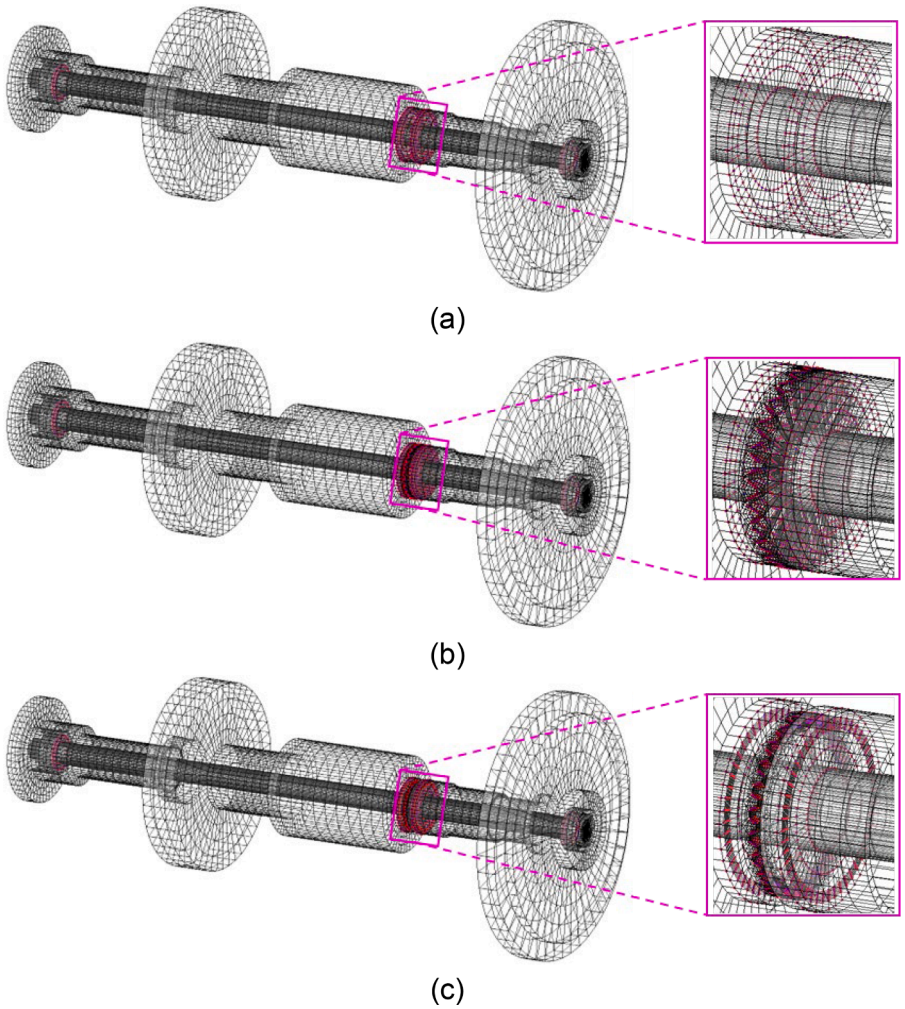

Fig. 30. The contact interfaces of the de Jongh rotor models with a (a) butt joint, (b) Hirth coupling, and (c) Curvic coupling.

Table 12
GW surface roughness parameters for the de Jongh rotor case study.

	R_s [m]	η_s [1/m^2]	σ_s [m]
Sigma1	1.0E-06	1.0E+10	1.0E-06
Sigma2	1.0E-06	1.0E+10	2.0E-06
Sigma3	1.0E-06	1.0E+10	3.0E-06

Sigma1. This indicates the predicted critical speeds for the 3D solid element and equivalent beam models show good agreement for the three coupling types. The relative difference between the Timoshenko beam and the 3D solid element Hirth coupling models at a preload of 5 kN with Sigma1 surface roughness is 41%. In comparison, the relative difference between the equivalent beam model and the 3D solid element Hirth coupling model is only 3%.

7. Conclusion

A novel equivalent beam modeling approach with lower computational requirements and improved accuracy was presented by combining the results of high fidelity 3D solid element modeling into a beam model. A review of Timoshenko beam theory was provided to explain the transverse shear effect $\Phi_{coupling}$, which is varied to match response the beam and solid element responses. The GW and amplitude parameters were reviewed, and linear relationships between them were inferred using linear regression. The coefficient of determination R^2 for the linear regression was found to be 99.8%.

The equivalent beam model was obtained by including the equivalent Young's modulus $E_{coupling}$ and equivalent transverse shear

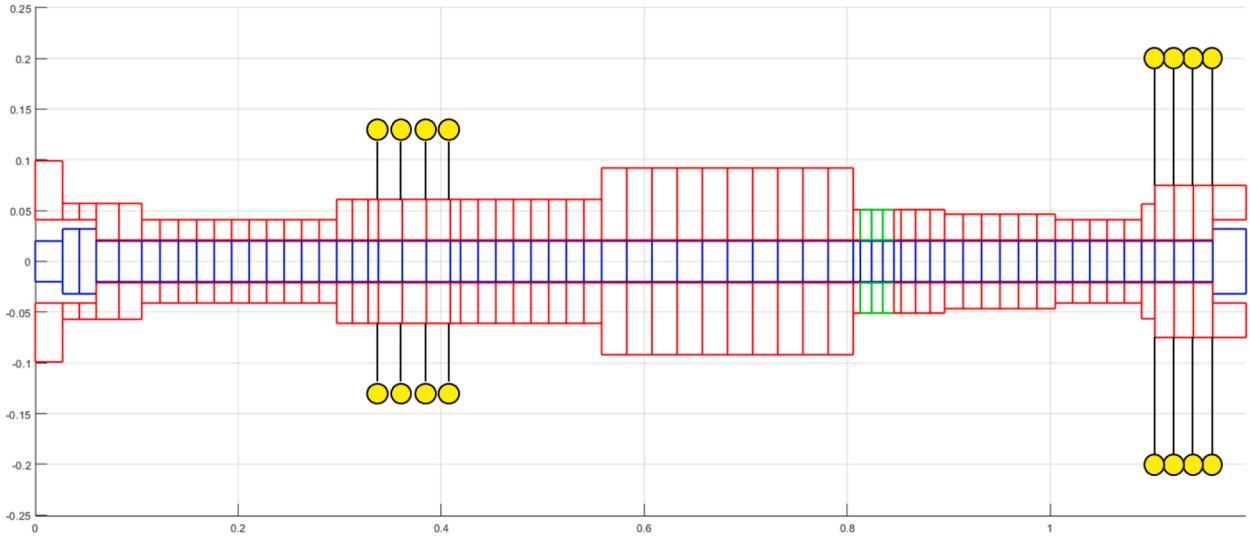

Fig. 31. Lumped inertia - beam model of the de Jongh rotor.

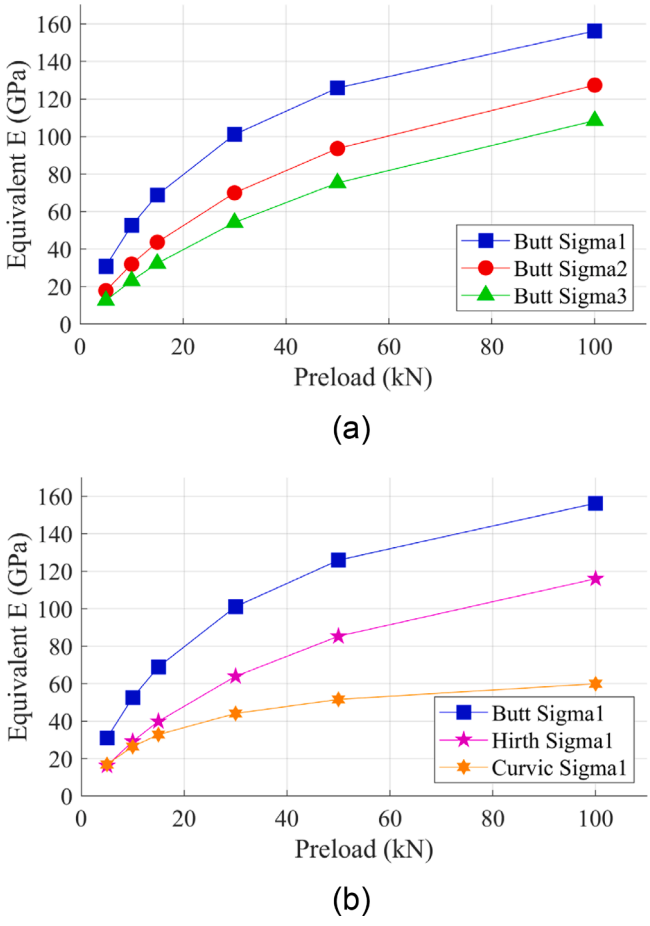

Fig. 32. $E_{coupling}$ vs. preload in de Jongh rotor for (a) different surface roughness of the butt joint and (b) different types of couplings with the same surface roughness.

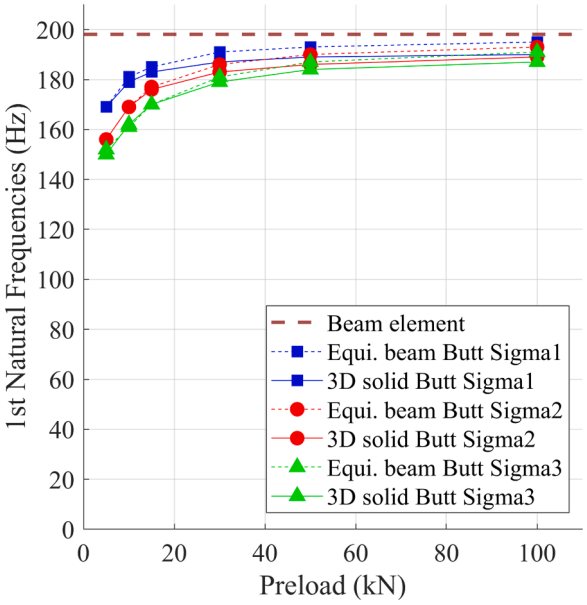

Fig. 33. Predicted free-free first bending mode natural frequencies of 3D solid, equivalent beam, and Timoshenko beam element with lumped mass for de Jongh rotor with different surface roughness on butt joint.

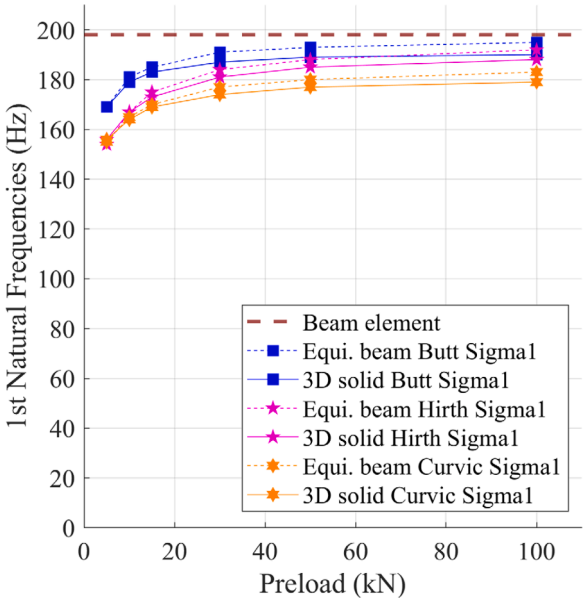

Fig. 34. Predicted free-free first bending mode natural frequencies of the 3D solid element, equivalent beam, and Timoshenko beam with lumped mass models for the de Jongh rotor with butt, Hirth, and Curvic couplings surface roughness Sigma 1.

effect $\Phi_{coupling}$ to reduce differences in the first and second mode frequencies, as predicted with beam and high fidelity solid element with asperity effect models. This is performed by simulation with rigid shaft members sandwiching the flexible coupling-joint. This isolates the flexible coupling of interest yielding its equivalent model to be used in any subsequent rotor model and any conventional rotordynamic simulation. The $E_{coupling}$ and $\Phi_{coupling}$ values adjusts a beam element model to account for the contact asperity effect. The accuracy of this approach was validated for various axial contact models with butt joints, and Hirth, and Curvic couplings. Validation was confirmed by comparing the beam and solid element model natural frequencies with each other and with test data. Use of the equivalent beam element approach reduced the beam model error for the butt joint case from 44.3% to 1.9% by incorporating the equivalent beam properties for the coupling beam elements. The results for the Curvic coupling case showed similar levels of prediction accuracy improvement.

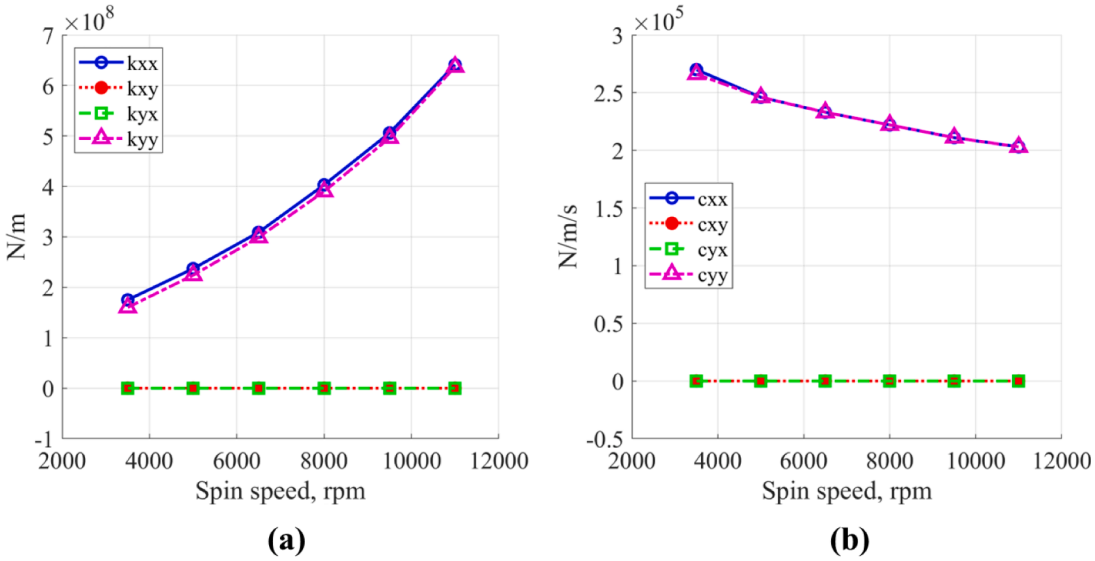

Fig. 35. (a) Stiffness and (b) Damping coefficients for the de Jongh rotor tilting pad bearings.

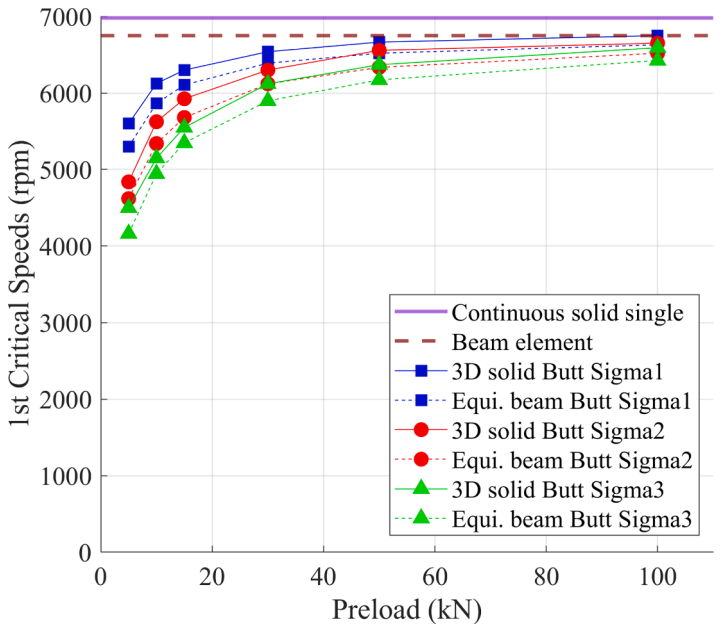

Fig. 36. Predicted first critical speeds of 3D solid element, equivalent beam, Timoshenko beam with lumped mass, and continuous 3D solid single model for the de Jongh rotor with different surface roughness on the butt joint.

The proposed modeling approach was demonstrated on an industrial rotor example to illustrate the methodology and results. A complete 3D solid element model of the rotor including asperity effects at the coupling contact surfaces, was treated as a benchmark for comparing the equivalent beam model. The results showed improved prediction accuracy of the equivalent beam approach relative to a standard beam element model approach for predicting natural frequencies and critical speeds. This was confirmed for the three coupling types and 3 levels of asperity roughness.

CRediT authorship contribution statement

Baik Jin Kim: Conceptualization, Methodology, Software, Investigation, Validation, Formal analysis, Writing – original draft. **Joseph Oh:** Methodology, Software, Investigation. **Alan Palazzolo:** Conceptualization, Methodology, Validation, Investigation, Resources, Writing – review & editing, Supervision, Project administration, Funding acquisition.

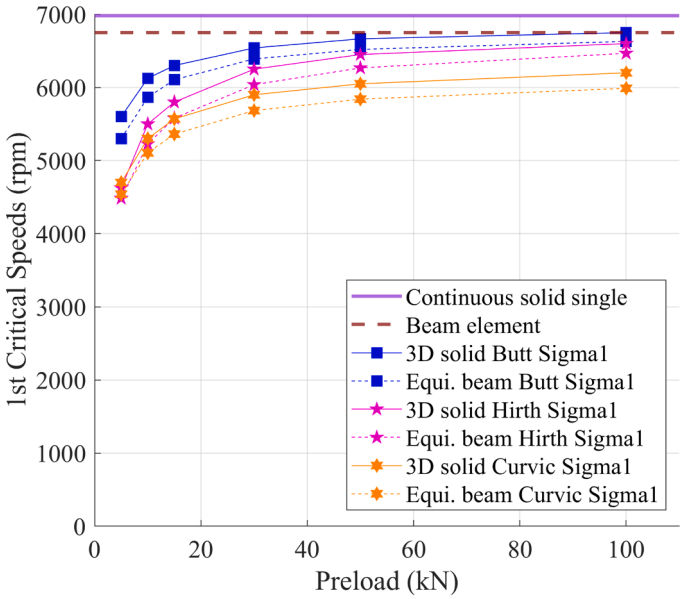

Fig. 37. Predicted first critical speeds of 3D solid element, equivalent beam, and Timoshenko beam element with lumped mass for de Jongh rotor with butt joint, Hirth, and Curvic coupling and same surface roughness.

Table A.1
The Local Coordinate, 3D Timoshenko Beam Stiffness Matrix* $\underline{\widetilde{K}}_e$.

Entries	Term
(1,1), (7,7), (−7,−1)	$\frac{EA}{L}$
(4,4), (10,10), (−10,−4)	$\frac{GJ}{L}$
(2,2) (8,8), (−8,−2)	$\frac{12\beta^a_{12}}{L^3}$
(6,2), (−8,−6), (12,2), (−12,−8)	$\frac{6\beta^a_{12}}{L^2}$
(6,6), (12,12)	$\frac{\beta^b_{12}}{L}$
(12,6)	$\frac{\beta^c_{12}}{L}$
(3,3), (9,9), (−9,−3)	$\frac{12\beta^a_{13}}{L^3}$
(−5,−3), (9,5), (−11,−3), (11,9)	$\frac{6\beta^a_{13}}{L^2}$
(5,5), (11,11)	$\frac{\beta^b_{13}}{L}$
(11,5)	$\frac{\beta^c_{13}}{L}$

* The matrix is symmetric $\underline{\widetilde{K}}_e^T = \underline{\widetilde{K}}_e$
All undefined terms in the 12 × 12 matrix are zero Negative entries (in parentheses) in the left column indicate to use the negative of the term shown in the right column.

Table B.1
Properties of the test rotor assembly with the Hirth coupling [19].

	OD (mm)	*ID* (mm)	*L* (mm)	Mass (g)	*P* (kg/m^3)	*E* (GPa)	ν
Through-bolt	19	0	381	780	7936	210	0.3
Nut	33	19	16	70	7682	210	0.3
Washer	38.1	20.92	3.9	24	8066	210	0.3
Outer shaft	50.8	25.4	152.4	1805	8523	210	0.3
Hirth coupling	49	20	20.55	88	8295	210	0.3

Table B.2
Properties of the Curvic test rotor assembly with the Curvic coupling *[4]*.

	OD (mm)	*ID* (mm)	*L* (mm)	Mass (g)	*P* (kg/m^3)	*E*(GPa)	ν
Through-bolt	22	0	381	1030	7112	200	0.3
Nut	34	22	20	103	7238	200	0.3
Washer	44	23.5	4	32	7361	200	0.3
Outer shaft	50.8	25.4	153	1813	7795	200	0.3
Curvic coupling	50.8	25.4	20	180	7800	200	0.3

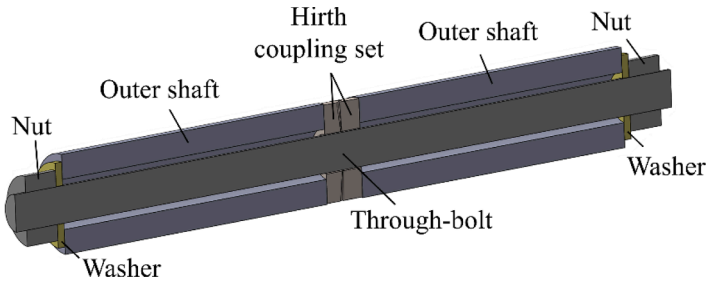

Fig. B.1. Test rotor assembly with Hirth coupling [19].

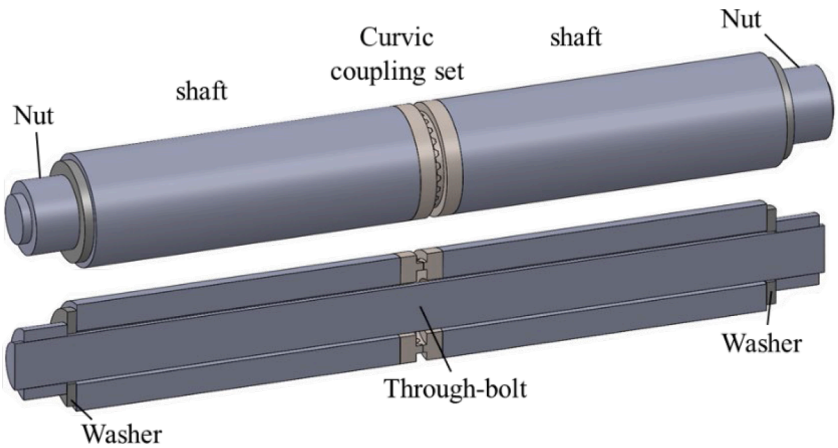

Fig. B.2. Test rotor assembly with Curvic coupling [4].

Declaration of Competing Interest

The authors declare that they have no known competing financial interests or personal relationships that could have appeared to influence the work reported in this paper.

Data availability

Data will be made available on request.

Acknowledgments

The authors would like to gratefully acknowledge funding for this work from the Texas A&M Turbomachinery Research Consortium (TRC). The authors would also like to thank the High Performance Research Computing Center at Texas A&M University.

Appendix A. Timoshenko beam element stiffness matrix [23]

$$\beta_{12}^{a} = \frac{EI_{\bar{x}_3}}{1+\Phi_{12}},\ \beta_{13}^{a} = \frac{EI_{\bar{x}_2}}{1+\Phi_{13}}$$

$$\beta_{12}^{b} = (4+\Phi_{12})\beta_{12}^{a},\ \beta_{13}^{b} = (4+\Phi_{13})\beta_{13}^{a}$$

$$\beta_{12}^{c} = (2-\Phi_{12})\beta_{12}^{a},\ \beta_{13}^{c} = (2-\Phi_{13})\beta_{13}^{a}$$

$$\Phi_{12} = \frac{12EI_{\bar{x}_3}}{k_2AGL^2} = \frac{24I_{\bar{x}_3}(1+\nu)}{k_2AL^2},\ \Phi_{13} = \frac{12EI_{\bar{x}_2}}{k_3AGL^2} = \frac{24I_{\bar{x}_2}(1+\nu)}{k_3AL^2}$$

The element stiffness matrix of Timoshenko beam [12 × 12] is expressed in tabular form in Table A.1.

Appendix B. Properties of the test rotor assembly with the Hirth, and Curvic coupling

The geometry and material properties of the test rotor assembly in Figs. 19 and 23 are shown in the tables below.

References

[1] A.M. Rimpel, M. Leopard, Simple contact stiffness model validation for tie bolt rotor design with butt joints and pilot fits, J. Eng. Gas Turbine Power 142 (1) (2020), 011014.
[2] Y. Liu, Q. Yuan, Z. Zhou, Contact status analysis of rod-fastened rotors with hirth coupling in gas turbines, in: Proceedings of the Turbine Technical Conference and Exposition, Montreal, Canada, 2015.
[3] G. Works, Curvic Coupling Design, Rochester, New York, 1986.
[4] B.J. Kim, J. Oh, A. Palazzolo, An improved preloaded curvic coupling model for rotordynamic analyses, J Sound Vib 544 (2023).
[5] G. Vannini, Rotordynamic validation of an ultra high speed multistage centrifugal compressor stacked rotor, in: Proceedings of the ASME Turbo Expo2014: Turbine Technical Conference and Exposition, Duesseldorf, Germany, 2014.
[6] J.A. Greenwood, J.B.P. Williamson, Contact of nominally flat surfaces, Proc. R. Soc. A Math. Phys. Eng. Sci. 295 (1442) (1966) 300–319.
[7] W.R. Chang, I. Etsion, D.B. Bogy, An elastic-plastic model for the contact of rough surfaces, J. Tribol. 109 (2) (1987) 257–263.
[8] M.R. Brake, An analytical elastic-perfectly plastic contact model, Int. J. Solids Struct. 49 (22) (2012) 3129–3141.
[9] D.J. Whitehouse, The properties of random surfaces of significance in their contact, Proc. R. Soc. A Math. Phys. Eng. Sci. 316 (1524) (1970) 97–121.
[10] J. Gao, Q. Yuan, P. Li, Z. Feng, H. Zhang, Z. Lv, Effects of bending moments and pretightening forces on the flexural stiffness of contact interfaces in rod-fastened rotors, J. Eng. Gas Turbine Power 134 (10) (2012), 102503.
[11] H. Peng, Z. Liu, G. Wang, M. Zhang, Rotor dynamic analysis of tie-bolt fastened rotor based on elastic-plastic contact, in: Proceedings of the ASME Turbo Expo 2011, Vancouver, British Columbia, Canada, 2011.
[12] M. Zhuo, L.H. Yang, L. Yu, Contact stiffness calculation and effects on rotordynamic of rod fastened rotor, in: Proceedings of the ASME 2016 International Mechanical Engineering Congress and Exposition, Phoenix, Arizona, USA, 2016.
[13] Y. Kim, S. Han, Y. Kim, Verification of rotordynamic design using 1/5 scaled model rotor of 270 MWclass gas turbine CenterTied rotor, Int. J. Precis. Eng. Manuf. 22 (2021) 271–285.
[14] H. Liu, J. Hong, D. Zhang, Bending and vibration of a discontinous beam with a curvic coupling under different axial forces, Front. Mech. Eng. 15 (3) (2020) 417–429.
[15] Y. Zhang, Z. Du, L. Shi, S. Liu, Determination of contact stiffness of rod-fastened rotors based on modal test and finite element analysis, J. Eng. Gas Turbine Power 132 (9) (2010), 094501.
[16] D. Croccolo, M.D. Agostinis, S. Fini, G. Olmi, F. Robusto, N. Vincenzi, On Hirth Ring Couplings Design Principles including the effect of friction, Actuators 7 (4) (2018) 79.
[17] X. Liu, Q. Yuan, Y. Liu, J. Gao, Analysis of the stiffness of hirth couplings in rod-fastened rotors based on experimental modal parameter identification, in: Proceedings of the ASME Turbo Expo2014: Turbine Technical Conference and Exposition, Duesseldorf, Germany, 2014.
[18] J. Oh, B.J. Kim, A. Palazzolo, Three-dimensional solid finite element contact model for rotordynamic analysis: experiment and simulation, J. Vib. Acoust. 143 (3) (2020), 031007.
[19] B.J. Kim, J. Oh, A. Palazzolo, Test and theory for a refined structural model of a Hirth coupling, ASME. J. Eng. Gas Turbines Power (2021).
[20] A. Tabenkin, The ABCs of Rz, Qual. Mag. (2007) 40–43, 29 October.
[21] B.J. Kim, A. Palazzolo, M. Gharib, Drillstring simulator: a novel software model for stick–slip and bit-bounce vibrations, in: Proceedings of the International Mechanical Engineering Congress and Exposition, Virtual Conference, 2021. Online.
[22] H.D. Nelson, A finite rotating shaft element using timoshenko beam theory, J. Mech. Des. 102 (4) (1980) 793–803.
[23] A.B. Palazzolo, Vibration Theory and Applications with Finite Elements and Active Vibration Control, Wiley, Chichester, UK, 2016.
[24] G.R. Cowper, The shear coefficient in timoshenko's beam theory, J. Appl. Mech. 33 (2) (1966) 335–340.
[25] R.D. Cook, D.S. Malkus, M.E. Plesha, R.J. Witt, Concepts and Applications of Finite Element Analysis, John Wiley & Sons. Inc., NJ, 2002.
[26] J. Oh, A.B. Palazzolo, L. Hu, Stability of non-axisymmetric rotor and bearing systems modeled with three-dimensional-solid finite elements, J. Vib. Acoust. 142 (1) (2020), 011010.
[27] J.A. Chaudhry, 3-D Finite Element Analysis of Rotors in Gas Turbines, Steam Turbines and Axial Pumps Including Blade Vibrations, Charlottesville, VA: Ph.D. thesis, University of Virginia, 2011.
[28] J.I. McCool, Comparison of models for the contact of rough surfaces, Wear 107 (1) (1986) 37–60.
[29] B. Bhushan, Contact mechanics of rough surfaces in tribology: multiple asperity contact, Tribol. Lett. 4 (1) (1998) 1–35.
[30] E..T. Whittaker, G.N. Watson, A Course of Modern Analysis, 4th ed., Cambridge University Press, Cambridge, UK, 1996.
[31] J. Lucietti, A class of identities relating Whittaker and Bessel functions, J. Math. Anal. Appl. 296 (1) (2004) 1–7.
[32] M. Abramowitz, I.A. Stegun, Handbook of Mathematical Functions, General Publishing Company, Ltd., Toronto, Ontario, 1965.
[33] H.A. Sherif, S.S. Kossa, Relationship between normal and tangential contact stiffness of nominally flat surfaces, Wear 151 (1) (1991) 49–62.
[34] E.S. Gadelmawla, M.M. Koura, T.M. Maksoud, I.M. Elewa, H.H. Soliman, Roughness parameters, J. Mater. Process. Technol. 123 (1) (2002) 133–145.
[35] R.G. Budynas, J.K. Nisbett, Shigley's Mechanical Engineering Design, McGraw-Hill, New York, NY, USA, 2008.

[36] F.M. de Jongh, Application of a Heat Barrier Sleeve to Prevent Synchronous Rotor Instability, Turbomachinery and Pump Symposia, 1998.
[37] A.C. Balbahadur, R.G. Kirk, Part II - case studies for a synchronous thermal instability operating in overhung rotors, Int. J. Rotat. Mach. 10 (6) (2004) 477–487.
[38] R.J. Guyan, Reduction of stiffness and mass matrices, AIAA J. 3 (2) (1965) 380.
[39] J. Yang, A.B. Palazzolo, Three-dimensional thermo-elasto-hydrodynamic computational fluid dynamics model of a tilting pad journal bearing—part II: dynamic response, J. Tribol. 141 (6) (2019), 061703.